
Draft Manuscript for Review

# Generation and rejuvenation of a supervolcanic magmatic system: a case study from Mangakino volcanic centre, New Zealand

| | |
|---|---|
| Journal: | *Journal of Petrology* |
| Manuscript ID | JPET-Aug-15-0095.R1 |
| Manuscript Type: | Original Manuscript |
| Date Submitted by the Author: | n/a |
| Complete List of Authors: | Cooper, George; Durham University , Department of Earth Sciences<br>Wilson, Colin; Victoria University, School of Geography, Environment and Earth Sciences<br>Millet, Marc-Alban; Durham University, Department of Earth Sciences<br>Baker, Joel; The University of Auckland, School of Environment |
| Keyword: | magma chamber, Kidnappers eruption, Rocky Hill eruption, supereruption, trace elements, rhyolite , Taupo Volcanic Zone |
| | |

# Generation and rejuvenation of a supervolcanic magmatic system: a case study from Mangakino volcanic centre, New Zealand

George F. Cooper[1,2]*, Colin J.N. Wilson[1], Marc-Alban Millet[1,,2] Joel A. Baker[3]

[1]School of Geography, Environment and Earth Sciences, Victoria University of Wellington, PO Box 600, Wellington 6140, New Zealand

[2]Present Address: Department of Earth Sciences, Durham University, Science Labs, Durham DH1 3LE, UK

[3]School of Environment, The University of Auckland, Private Bag 92019, Auckland, New Zealand

*corresponding author:

email: george.cooper@durham.ac.uk

phone: +44 7739525205

fax: +44 0191 3342301

Keywords: Kidnappers eruption; magma chamber; Rocky Hill eruption; supereruption; trace elements; rhyolite

## ABSTRACT

The Kidnappers (~1200 km$^3$, DRE) and Rocky Hill (~200 km$^3$, DRE) caldera-forming events (Taupo Volcanic Zone, New Zealand) were erupted in close succession from the Mangakino volcanic centre. They have identical radiometric ages at ~1 Ma, yet erosion along the contact between the two deposits suggest that some years to decades separated the two eruptions. Field constraints, and the similarities of crystal textures and compositions and glass chemistries of both eruption deposits demonstrate that they came from one overall magmatic system with a common crystal mush source. However, second-order variations in these parameters confirm that the Kidnappers and Rocky Hill deposits represent distinct events and are not the products of a single zoned magma chamber. The systematically zoned Kidnappers fall deposits provide evidence for the tapping of three discrete magma bodies, whereas the succeeding Kidnappers ignimbrite is compositionally more diverse. The transition from fall to flow deposition marks a change in the style of caldera collapse and the simultaneous evacuation of discrete but compositionally diverse melts, each of which underwent a distinct evolution and were held at slightly different P–T conditions prior to eruption. Contrasting plagioclase and orthopyroxene zonation patterns are present from pumices originating from three discrete magma bodies. Less evolved mafic melts interacted with the system, which mobilised portions of the final erupted melt through heating and volatile/chemical exchange in the mush. The two largest Kidnappers melt-dominant bodies were re-tapped in modified form, or reestablished from their common mush source prior to, the Rocky Hill event. Rocky Hill pumices contain common, fluid-affected antecrystic crystal clots, derived from chamber wall material. Amphibole compositions from each eruption reflect melt evolution processes and, in particular, the coeval crystallisation of biotite and breakdown of orthopyroxene. Plagioclase and orthopyroxene from Rocky Hill pumices share common zonation patterns with those from the two largest magma bodies in the Kidnappers. The rapid production of

new melt-dominant bodies and the triggering of the Rocky Hill eruption reflect the ability of the magmatic system to rejuvenate on a geologically short timescale. The Mangakino centre did not follow a typical cycle of decreased activity after the supervolcanic Kidnappers event, instead producing a second caldera-forming eruption, within years to decades from the same system.

## INTRODUCTION

Reconstructing the processes that occur in silicic (dacite and rhyolite) magma systems prior to and during supereruptions (>$10^{15}$ kg ≈ 450 $km^3$ of magma erupted; e.g. Miller & Wark, 2008), and understanding how such vast parental bodies of magma are generated, stored and ultimately erupted is challenging. Concepts of the nature and storage conditions of large silicic magma bodies, and how a chemical zonation (if any) is developed within these magma systems vary widely (e.g. Cashman & Giordano, 2014). Hildreth (1981) proposed the classic high-silica rhyolite magma chamber paradigm, where any chemical or physical magma chamber zonation is inversely reflected in the eruption products (Smith, 1979; Bachmann & Bergantz, 2008). This model was largely based on compositional variations observed within the Bishop Tuff (Hildreth, 1979), reflecting eruption of earlier crystal-poor, more evolved magmas, followed by crystal-rich, less evolved magmas, with gradients in crystal content matching those in chemical and mineralogical properties (Hildreth & Wilson, 2007; Chamberlain *et al*., 2015). Many large Quaternary rhyolitic deposits in the Taupo Volcanic Zone (TVZ) of New Zealand show significant compositional variations (e.g. Briggs *et al*., 1993; Brown *et al*., 1998a, Milner *et al.,* 2003; Wilson *et al.,* 2006; Cooper *et al.,* 2012; Allan *et al.,* 2013; Bégué *et al*., 2014). These variations are, however, often non-systematic: erupted compositions may be reversely ordered, or be distributed such that multiple discrete magma bodies are inferred to have been tapped within single eruptive events, both large (Gravley *et*

*al.,* 2007; Cooper *et al*., 2012; Bégué *et al*., 2014) and small (Nairn *et al.,* 2004; Shane *et al.*, 2007, 2008a, b). Additionally, with the possible exception of Toba (Chesner, 2012), caldera-forming eruptions are not isolated, but are coupled with other, smaller (by one or more orders of magnitude) pre- and post-caldera eruptions from a common magmatic focus. At one extreme, a precursor leak occurred only ~3 kyr prior to the 25.4 kyr Oruanui supereruption in New Zealand, then there was only ~5 kyr of quiescence before frequent eruptive activity resumed (e.g. Wilson & Charlier, 2009; Barker *et al*., 2015). Other examples of smaller-scale pre- and post-caldera activity include Yellowstone (Girard & Stix, 2010; Pritchard & Larson, 2012; Watts *et al.,* 2012), Valles caldera, New Mexico (Smith & Bailey, 1966; Self *et al.,* 1986; Stix *et al*., 1988; Wolff *et al.,* 1999*,* 2011; Kennedy *et al.,* 2012), and Long Valley caldera (Metz & Mahood, 1985, 1991; Hildreth, 2004).

In each of these systems, pre- and post-caldera-forming activity on short timescales (thousands to tens of thousands of years) is modest in volume. A notable contrast to these examples, however, is the 1 Ma (Houghton *et al*., 1995; Wilson *et al*., 1995a) Kidnappers and Rocky Hill caldera-forming eruptions from Mangakino volcanic centre in the TVZ, which were erupted in close succession from a common source (Wilson, 1986; Wilson *et al*., 2008). Zircon U–Pb age spectra in pumices from the two eruptions are closely similar, suggesting that zircon growth occurred within a common magmatic system over a period of ~200 kyr, with two peaks in zircon crystallisation about 100 kyr before and immediately prior to eruption, respectively (Cooper *et al*., 2014). The two sets of deposits collectively provide windows into the short-term processes involved in the development and immediately post-eruptive state of a supervolcanic magmatic system.

The Kidnappers and Rocky Hill deposits also highlight issues in the material available for analysis to interrogate the compositional record in large silicic eruptions. Stratigraphically ordered fall deposits can be used to track compositional variations through time within and

between eruptions (e.g., Snake River Plain rhyolites; Perkins & Nash, 2002; Cathey & Nash, 2004). However, sufficiently large pumice clasts for individual analysis are absent in the Kidnappers fall deposits, and therefore the inter-relationships between mineral, glass and whole-rock compositions cannot be easily studied. Conversely, the Kidnappers and Rocky Hill ignimbrites, although poorly exposed and lacking all but the broadest of stratigraphic controls (e.g. the latter overlies the former), contain fresh pumices large enough to permit the whole-rock, glass and mineral relationships of individual clasts to be explored.

Here, we present geochemical and petrological data from the Kidnappers fall deposit, and the Kidnappers and Rocky Hill ignimbrites in order to compare and contrast the deposits and reconstruct their magmatic sources. Matrix glass from pumices within the Kidnappers and Rocky Hill ignimbrites is compared to the three glass types previously identified in the Kidnappers fall deposit (Cooper *et al.,* 2012). New mineral compositional data from the fall deposit (organised by stratigraphic ordering) are compared alongside the data from ignimbrite pumices (organised by major element chemistry), providing a record through the full (preserved) stratigraphic history of the parental eruptions. The following questions are addressed: (1) Can the distinction made between these eruptions from field evidence be observed in the minerals and glasses, or geochemically and mineralogically do the Kidnappers and Rocky Hill deposits appear to be phases of a single eruption? (2) How many melt compositions were involved in the Kidnappers and Rocky Hill eruptions, and how were they stored, and were they mixed? (3) Is evidence present in the geochemical and mineralogical data to support inferences from zircon U–Pb age spectra (Cooper *et al*., 2014) that the Kidnappers and Rocky Hill deposits were derived from a common system? (4) Are there any geochemical signatures present within the eruption deposits to give insights into potential triggering mechanisms and rejuvenation processes? (5) Did conditions operating

within the magmatic system (in particular temperature, pressure, oxygen fugacity and $H_2O$ contents) remain constant or change between eruptive events?

## GEOLOGICAL BACKGROUND

The TVZ is a NNE-trending locus of volcanism and associated extension forming the southern, continental termination of the Tonga–Kermadec arc, itself associated with westward subduction of the Pacific plate beneath the Indo–Australian plate (Cole & Lewis, 1981). The TVZ has been the dominant focus of volcanism in the central North Island of New Zealand since ~2 Ma, and is divided into three segments on the basis of the dominant magma composition and magma fluxes. Within the ~120 × 60 km rhyolite-dominated central segment, >16,000 $km^3$ of magma has been erupted since ~1.6 Ma in >25 caldera-forming and numerous other smaller eruptions from eight volcanic centres (Houghton *et al.,* 1995; Wilson *et al.,* 1995b, 2009). The Mangakino volcanic centre (MVC; Fig. 1) on the northwestern margin of the TVZ was recognised from the presence of a major negative gravity anomaly, in addition to geological field evidence that linked several ignimbrites to a source in this area (Blank, 1965; Stern, 1979; Rogan, 1982; Wilson *et al.,* 1984; Wilson, 1986). The MVC is a composite feature, activity from which is grouped into two periods of caldera-forming eruptions (Houghton *et al.,* 1995), from 1.62–1.51 Ma and 1.21–0.91 Ma. The latter period includes the Kidnappers and Rocky Hill eruptions, as well as the 1.21 Ma Ongatiti supereruption (Briggs *et al*., 1993; Cooper & Wilson, 2014).

The Kidnappers and Rocky Hill eruptions are dated at ~1 Ma by $^{40}Ar/^{39}Ar$ techniques on plagioclase, and constrained by their position towards the top of the Jaramillo Normal Subchron (1.07-0.99 Ma) (Black, 1992; Houghton *et al.,* 1995; Wilson *et al.,* 1995a; Tanaka et al., 1996; Singer, 2014). The Kidnappers is the second largest TVZ eruption known (1200 $km^3$ ± 50%, DRE; Cooper *et al.,* 2012) and it generated three components: (1) a voluminous

phreatomagmatic fall deposit, recorded across the North Island and for >1000 km eastwards across the Pacific Ocean floor (Ash A of Ninkovich, 1968; Carter *et al.,* 2004; Cooper *et al.,* 2012); (2) an exceptionally widespread non-welded ignimbrite that covers ~45000 $km^2$ (Wilson *et al.,* 1995a; Fig. 1); and (3) >1.3 km of poorly welded, hydrothermally altered tuff deposited within the inferred source collapse structure (Wilson *et al.,* 2008). Geochemical investigations of the fall deposit showed that three laterally separated magma chambers were sequentially tapped during the volumetrically dominant earlier stages of the Kidnappers eruption, within what became an inferred common composite caldera (Cooper *et al.,* 2012).

The Kidnappers eruption was followed by a short period of quiescence before eruption of the Rocky Hill ignimbrite (~200 $km^3$, DRE), which extends to at least 85 km from source (Briggs *et al.,* 1993; Fig. 1). The ignimbrite grades from a partially welded, pumice- and crystal-rich base to a densely welded upper part with lower pumice abundance (Blank, 1965; Wilson, 1986; Moyle, 1989). In addition, >0.5 km of Rocky Hill ignimbrite was penetrated by drillholes within the Mangakino composite collapse caldera (Wilson *et al.,* 2008; Cooper *et al*., 2014). Zircon U–Pb age spectra from both Kidnappers and Rocky Hill pumices define two modes at 1.1 and 1.0 Ma (Cooper *et al*., 2014), inferred to represent two periods of enhanced crystallization: first, in a common magmatic source (‘mush’) zone and second, in the melt dominant bodies shortly prior to or interrupted by eruption, respectively. In the field, the welded Rocky Hill ignimbrite forms crags and large boulder exposures (Blank, 1965), but the Kidnappers deposits are only exposed in slip scars or road cuttings (Fig. 2). Although the relevant contact is very rarely exposed, a time break between them is represented by erosional reworking (but not soil development) of the top of the Kidnappers ignimbrite before emplacement of the Rocky Hill ignimbrite (Fig. 2). In addition, the Rocky Hill ignimbrite is sometimes observed to rest on older rocks from which the Kidnappers deposits have been stripped. A period of years to decades between eruptions is thus inferred, based on

observations that vegetation regrowth and incipient soil development on thick deposits under New Zealand interglacial climate conditions could be expected to show up after about 50-100 years (e.g. Turner, 1928; Wilson, 1993). It is also inferred from glass compositions (Cooper *et al.,* 2012) and field characteristics that the Kidnappers and Rocky Hill eruptions collectively contributed to a composite deposit of primary and reworked volcaniclastic material that is mapped widely throughout New Zealand as the Potaka Tephra (e.g., Shane, 1994; Carter *et al.,* 2004; Alloway *et al.,* 2005).

## SAMPLING

Sampling of the Kidnappers fall deposit is discussed in Cooper *et al.* (2012). The majority of Kidnappers pumices were sampled from pumice-rich, non-welded to sintered ignimbrite in a quarry near Litchfield (38.108563°S, 175.836467°E), ~30 km from source, and others from a farm pumice pit at 37.848558°S, 175.704651°E (Fig. 1). At both sites the ignimbrite is >10 m thick, and contains pumices up to ~60 cm long. Kidnappers pumice is typically light grey-buff in colour and contains discrete crystals (rather than crystal clots). Biotite is visibly present in the majority of pumice clasts (although commonly weathered to a golden hydromica, which is also obvious in the matrix), and pumices have a remarkably similar physical appearance throughout the sampled ignimbrite.

Rocky Hill pumices were sampled from several locations of indurated to poorly welded ignimbrite west of Mangakino within the Waipa Valley (Fig. 1), ~50 km from source, at 38.437617°S, 175.363719°E and 38.404997°S, 175.343761°E. The eponymous Rocky Hill type locality (Martin, 1961; Blank, 1965) was sampled at 38.381729°S, 175.308160°E and 38.382241°S, 175.308460°E. Most Rocky Hill pumice is glomeroporphyritic, with both spherical crystal clots (commonly with brown glass selvedges) and schlieren. Large (up to 4–5 mm) amphibole phenocrysts are ubiquitous within Rocky Hill pumice and biotite, whilst

present, is sparse. The overall colour of pumice clasts varies from white (~70%) to dark grey or brown (~30%), either with or without colour streaking.

## ANALYTICAL TECHNIQUES

These are summarised here, with full details presented in the Supplementary Information. Analyses of reference standards used to demonstrate the overall reproducibility and accuracy of the data are also presented in Supplementary Data.

Whole-rock major element analyses were carried out by X-ray fluorescence (XRF) spectrometry using Philips PW2400 Sequential Wavelength Dispersive X-ray Fluorescence Spectrometers at the University of Canterbury and Spectrachem Analytical (CRL Energy Ltd), Lower Hutt. Whole-rock trace element analyses were carried out by solution inductively coupled plasma mass spectrometry (ICP-MS), using an Agilent 7500cs ICP-MS at Victoria University of Wellington.

Backscattered electron (BSE) imaging and quantitative major element analyses of glass and crystals were carried out using a JEOL JXA-8230 Superprobe at Victoria University of Wellington. Minerals were analysed with a 15 kV accelerating voltage and a 12 nA focused beam. Glass was analysed with a 15 kV accelerating voltage and an 8 nA beam current with a defocused beam (20 μm). Trace element compositions of minerals and glass were determined using a New Wave deep UV (193 nm solid state) laser ablation system coupled to a Agilent 7500cs ICP-MS at Victoria University of Wellington. All data were acquired as static spot analyses with a beam diameter of 35 μm, a laser repetition rate of 5 Hz, 85% laser power and using helium as the carrier gas.

## RESULTS

The Kidnappers fall matrix glass data were presented in Cooper *et al.* (2012) and are used here as a basis for comparison between pumice matrix glass data from the overlying ignimbrites. Establishing variations in pumice matrix glass chemistry is essential when examining deposits such as the Kidnappers and Rocky Hill ignimbrites (where stratigraphic control is limited), so that crystal characteristics can be given additional context from the eruption deposits as a whole. All samples used for glass and crystal specific work in this study are listed in Fig. 3. All data used in this paper are presented in the supplementary electronic appendices.

**Whole-rock pumice compositions and glass chemistry**

Pumices within the Kidnappers (and to a lesser extent the Rocky Hill) deposits are of very similar physical appearance. End-member pumice types were first determined on the basis of their whole-rock chemistry before representative clasts were chosen for glass and crystal-specific analyses (Fig. 3). All pumices analysed show some degree of secondary hydration, with loss-on-ignition values of up to 5 wt.%. All reported whole-rock and glass major element data were normalized to an anhydrous basis.

*Kidnappers whole-rock pumice compositions*

Whole-rock major element data cluster into three different groups based on $SiO_2$, MgO, $TiO_2$ and CaO values (Fig. 4). The majority of Kidnappers ignimbrite (KI) pumices can therefore be divided into a dominant mid-$SiO_2$ type (KI-1: 72–74 wt.% $SiO_2$) a high $SiO_2$ variant (KI-2: >74.5 wt.% $SiO_2$) and a low $SiO_2$ variant (KI-3: <72 wt.% $SiO_2$) (Tables 1 and 2). Trace elements Ni, Zn, Sr and Zr behave compatibly with increasing $SiO_2$, whereas Ba and Rb behave incompatibly (Fig. 5), despite the abundance of biotite (for which both elements have Kd>1). Rb/Sr ratios within Kidnappers pumices range from 0.5 to 2.0 with elevated Rb/Sr

values in pumices with the highest $SiO_2$ content (KI-2), consistent with the accumulation of plagioclase (Fig. 5). Eu/Eu* ranges from 0.74–0.47 and decreases with decreasing $Al_2O_3$. The relative differences in the compositions of average Kidnappers matrix glass mirror those of the three whole-rock compositional groups (e.g. the low-$SiO_2$ whole-rock group corresponds to the low-$SiO_2$ glass group; Figs. 4 and 5). The variance of whole-rock pumice geochemistry is therefore influenced by the chemistry of the matrix glass i.e., the melt phase, in addition to reflecting the varying crystal cargo within each clast.

*Kidnappers pumice matrix glass compositions*

Eleven representative pumices covering all compositional groups from the Kidnappers ignimbrite were chosen for analysis of their matrix glass (Table 2). Tie-lines drawn between major element whole-rock and average matrix glass compositions have gradients in common with the overall whole-rock data, apart from $K_2O$ and $Na_2O$ which share a similar range in concentrations between whole-rock and glass (Fig. 4). Average matrix glass values range from 76.3–78.5 wt.% $SiO_2$, 3.4–4.6 wt.% $K_2O$ and 0.6–1.3 wt.% CaO, and the overall eruption products are characterised by glass heterogeneity (Fig. 6). Matrix glass within individual pumice samples from KI-1 and KI-2 is homogeneous with respect to major elements, apart from FeO that spans a range beyond analytical uncertainty in all clasts. However, matrix glasses from the two KI-3 pumices (Fig. 3) have major element heterogeneity beyond analytical uncertainties (Fig. 6). Trace element heterogeneity at a single pumice scale is particularly evident in elements highly compatible in plagioclase and zircon such as Sr and Zr, respectively (Fig. 6).

In addition to the aforementioned elemental variability, there are compositional gaps in matrix glass across the suite of analysed pumice samples (Fig. 6). The glass chemistry shows clustering into three groups (best defined by plots of $SiO_2$ versus CaO, or Zr versus

Th), which correspond in almost all cases to the three groups evident from whole-rock compositions (Fig. 4). Matrix glass from the KI-3 group shows separate, sub-parallel trends when compared to the KI-1 and KI-2 groups on all major and trace element plots (Fig. 6). Compositional fields covered by KI-1 and KI-2 glasses overlap and display the same slope in terms of FeO and Rb/Sr (Fig. 6). The three matrix glass groups within the Kidnappers ignimbrite pumices span a larger range than the three compositionally distinct glass types found in the underlying fall deposit (Cooper *et al.,* 2012; Fig. 6). KI-1 overlaps both the KF-A and KF-C (KF: fall deposit) compositional fields on all plots apart from $SiO_2$ vs. Mg, and extends to higher trace element concentrations (Zr, Sr, La and Th) (Fig. 6). KI-2 overlaps KF-B but extends to lower CaO and FeO concentrations as well as higher trace element concentrations (Zr, Sr, La and Th). KI-3 does not overlap any of the Kidnappers fall groups, and has significantly higher $Al_2O_3$ concentrations (~13.4 wt.%), therefore representing a magma apparently confined to later ignimbrite-forming stages of the Kidnappers eruption.

*Rocky Hill whole-rock pumice compositions*

In comparison to the Kidnappers whole-rock data, similar or larger (e.g., 65.0–76.2 wt.% $SiO_2$; 13.1–21.3 wt.% $Al_2O_3$; Fig. 7) major element variations are evident. $K_2O$ and $Na_2O$ concentrations are generally lower and higher, respectively, in Rocky Hill pumices as compared with Kidnappers pumices (Fig. 7). MgO concentrations are lower than those observed in Kidnappers pumice samples (Fig. 7d) at the less-evolved end of the compositional range (<71 wt.% $SiO_2$). Unlike in the Kidnappers pumices, a continuity of values is shown across the range in major element concentrations. Trace elements such as Ni, Zn, Sr and Zr behave compatibly whereas Rb behaves incompatibly (Fig. 8). Ba is less incompatible in the Rocky Hill than the Kidnappers samples (Fig. 8b). Rb/Sr ratios within Rocky Hill pumice span a more restricted range and form a sub-parallel trend to the

Kidnappers compositional array when plotted against $K_2O$ (Fig. 8). Eu/Eu* ratios cover a smaller range (0.76–0.53) with a sharp decrease observed in pumices with <16 wt.% $Al_2O_3$ (Fig. 8). Unlike the Kidnappers pumices, Y shows a more systematic relationship with $Al_2O_3$ with sub-parallel tie lines (Fig. 8f).

*Rocky Hill pumice matrix glass compositions*

Nine pumices from the Rocky Hill ignimbrite were chosen for matrix glass analysis on the basis of whole-rock composition (Fig. 3 and Tables 1 and 2). In general, tie-lines drawn between major element whole-rock and average matrix glass compositions have the same slopes (over similar lengths) as in the Kidnappers pumices, suggesting a similar degree of influence of the crystal content on pumice–glass relationships (Fig. 7). However, unlike in the Kidnappers pumices, $K_2O$ tie-lines have positive and $Na_2O$ tie-lines negative slopes with increasing $SiO_2$ (Fig. 7). Rocky Hill matrix glass has higher Rb/Sr and $K_2O$ values than its corresponding whole-rock value (Fig. 8) and displays less variation in major element chemistry than within the Kidnappers pumices (Fig. 9). The matrix glass within each pumice clast is homogeneous (within a 2 sd range) with respect to major elements, apart from FeO that ranges over 0.8 wt.% in each sample (Fig. 9). Two compositionally discrete matrix glass groups are present across the Rocky Hill (RH) pumice suite (best shown by Th vs. Zr: Fig. 9f), and therefore clasts are grouped into 'normal' (RH-1; higher CaO and lower $SiO_2$) and high-$SiO_2$ types (RH-2; lower CaO; Fig. 9a).

Although these groups reflect distinct matrix glass compositions, associated whole-rock compositions show a large range with no compositional gaps. An arbitrary value of 74 wt.% $SiO_2$ is therefore used to distinguish the RH-1 and RH-2 pumices. As in the Kidnappers pumice glass, heterogeneity within Rocky Hill pumice glass is more pronounced in trace elements, particularly Zr and Sr (Fig. 9). Matrix glass major-element compositions overlie the

KI-1 and KI-2 Kidnappers glass groups. Trace element concentrations from the dominant RH-1 type matrix glass overlie and extend the KI-1 Kidnappers glass group but do not show the same trends as the KI-3 group. Pumice samples P2029 and P2030 from group RH-1 (Fig. 3) have matrix glass Mg concentrations of <500 ppm, lower than any values within the Kidnappers products (Fig. 9d). Trace element concentrations within group RH-2 overlap the KI-2 group concentrations with respect to all elements. The two Rocky Hill glass groups form sub-parallel trends on plots of Sr versus La and Zr versus Th with limited or no overlap (Fig. 9f, g).

In many Rocky Hill pumices, particularly those of RH1 type, brown glass can be observed sheathing crystal clots (Supplementary Fig. 1). The brown glass is less vesicular and has thicker bubble walls than the matrix glass and is commonly compositionally distinct with, on average, higher $Na_2O$ (5.1 wt.%) and CaO (1.2 wt.%) but lower $K_2O$ (1.4 wt.%), Rb (66 ppm), Ba (716 ppm) and Li (19 ppm) than the matrix glass (Supplementary Fig. 1).

**Mineral textures**

All pumices analysed from both ignimbrites and the Kidnappers fall deposit contain a similar phenocryst assemblage, in decreasing order of abundance, of plagioclase + quartz + orthopyroxene + hornblende + magnetite + ilmenite, plus accessory zircon and apatite. Of the major phases, plagioclase (the dominant phase in all deposits) and orthopyroxene show distinct textural characteristics (core-rim zoning) and the differences between compositional groups and deposits are described below. Amphiboles do not display consistent textural core-to-rim relationships or systematic zoning patterns and it was not feasible to characterise these grains based on zoning visible in BSE imagery. However 10–20% of amphibole grains have patchy recrystallised cores, which may represent an antecrystic or xenocrystic component. Within Rocky Hill pumices, amphibole occurs distinctively as euhedral crystals up to 4–5 mm

long. Biotite appears part way through the Kidnappers fall deposit (in association with the KF-B-type glass: Cooper *et al*., 2012), is present in nearly all Kidnappers pumices, but is sparse within Rocky Hill pumices. In all cases, however, the biotite displays no clear BSE zoning patterns, is generally weathered in the Kidnappers deposits and is not described further below. Quartz is present throughout the Kidnappers fall deposit and within all Kidnappers and Rocky Hill pumices. Cathodoluminescence (CL) imaging, which largely reflects the concentration of Ti, reveals oscillatory zoned quartz grains, often with multiple resorption zones. Samples chosen for crystal specific analyses from each deposit are listed in Fig. 3 and characteristics of the mineral phases are summarised in Table 3.

*Kidnappers fall deposit mineral textures*

Mineral characteristics and accompanying compositions in the Kidnappers fall deposit, briefly discussed in Cooper *et al*. (2012), are presented here in more detail to allow comparisons with the two ignimbrites. Samples were collected from the most proximal (~30 km from the caldera rim) and thickest (4.0 m) section known of the Kidnappers fall deposit. The mineral assemblage at each sampled horizon (apart from the KF-A-dominant base) reflects a mixture of material from at least two compositional groups. Thus, crystals from the fall deposit cannot always be definitively matched with the glass compositional groups. In particular, crystals from KF-C cannot be separated out from the other groups and so KF-C material is presented within the 'other' group below (Fig. 3).

Around 25% of plagioclase at all stratigraphic heights displays patchy cores, often with a sieved texture (Tsuchiyama, 1985; Nelson & Montana, 1992). Plagioclase outermost rims at each analysed fall horizon (Fig. 3) are divided into three populations based on changes in BSE intensity between interior domains and outermost rims: light rims, dark rims, and non-distinct rims (that is, no tonal change, or fine oscillatory zoning to the outermost rim) (Fig. 10

and Supplementary Fig. 2). Grains displaying non-distinct rims are the dominant population (42–92%), and grains with light rims are subordinate at each stratigraphic horizon (3–12%). The most notable observation is the near absence of plagioclase with dark rims at the base of the deposit (where glass type KF-A dominates). This suggests that dark rimmed grains are characteristic of the KF-B compositional group which first appears ~1 m above the base of the deposit.

Orthopyroxene crystals at each analysed fall horizon (Fig. 3 and Supplementary Fig. 2) were classified into four populations based on simplified textural characteristics in BSE imaging: (1, 2) grains in which interiors follow general (1) normal and (2) reverse zoning patterns; (3) grains which are nominally unzoned; and (4) grains which have a patchy appearance with no clear zoning relationships (Fig. 11 and Supplementary Fig. 2). Reversely zoned grains are only present in any significant quantity (up to 25%) from just above the base to ~2 m height in the fall deposit (Fig. 3 and Supplementary Fig. 2). The least evolved, KF-C glass type is only found within the same horizons, suggesting that the reversely zoned grains are associated with the KF-C melt.

*Kidnappers ignimbrite pumice mineral textures*

Around 20% of plagioclase across all pumice types display patchy (often sieve textured) cores. Within KI-3 pumice, grains with light rims dominate (82%) and grains with dark rims are absent, whereas in KI-2 pumice 42% of grains have prominent dark rims and only 2% have light rims (Fig. 10). Within KI-1 pumice, non-distinct rims (66%) dominate over dark (12%) or light (22%) rims. The dominance of light-rimmed plagioclase in KI-3 is distinctive to the ignimbrite and not observed in the Kidnappers fall deposit (Supplementary Fig. 2).

Quartz grains within a single KI-2 pumice were imaged by CL and were classified into three groups: 80% of grains display dark rims, 7% light rims, and 13% have no significant compositional change at the rim.

Orthopyroxene crystals were classified into the same four populations as within the fall deposit. However, a further distinction can be made of crystals that show a dark exterior zone (Fig. 11). This dark zone can be superimposed onto each of the four textural groups described above and is either found within 100 μm of the outermost crystal rim, or as the outermost rim itself (Fig. 11). There is a high proportion (41%) of grains with a dark (high Mg) exterior zone found in KI-3 pumice as compared with only 2% and 6%, in KI-2 and KI-3 pumice samples, respectively (Fig. 11). Systematic changes are observed in the proportions of normally zoned, unzoned and reversely zoned types within each whole-rock compositional group (Fig. 11). Patchy grains, interpreted to reflect significant recrystallization, do not follow a particular trend and are generally subordinate to the other textural types.

*Rocky Hill ignimbrite pumice mineral textures*

Broken and/or exploded plagioclase crystals are common within the crystal clots, the broken crystals having textures like the 'phenoclasts' of Best and Christiansen (1997), surrounded by palisade bubble textures (Rotella et al., 2015). The fragments of exploded crystals are irregularly shaped, resembling a jigsaw, and held together by glass with large vesicles and thick bubble walls (Supplementary Fig. 1). A greater proportion (~30%) of Rocky Hill plagioclase displays patchy or sieve textured cores when compared to the Kidnappers. Plagioclase rim-type proportions are closely matched between the RH-1 and KI-1, and RH-2 and KI-2 groups (Fig. 10). No Rocky Hill pumices contain plagioclase where light rims dominate, in contrast to the KI-3 group (Fig. 10).

Quartz grains within a single RH-1 pumice were imaged by CL. In contrast to the Kidnappers, grains with light rims dominate (61%) over those with dark rims (19.5%) and those showing no change (19.5%).

Orthopyroxene crystals with normal zoning are 55% of the orthopyroxene population in RH-1 pumice, increasing to 94% in RH-2 pumice. Concurrently, unzoned grains decrease from 38% to 5%, and reversely zoned grains decrease from 7% to 1%, respectively (Fig. 11). Grains with a dark (high Mg) exterior zone decrease in abundance from 13% in RH-1 pumices to 1% in RH-2 pumices, parallel to the changes observed between KI-1 to KI-2 pumices in the Kidnappers ignimbrite (Fig. 11).

**Mineral chemistry**

Samples chosen for mineral chemical analysis are listed in Fig. 2 and the ranges in compositions of crystal phases from each of the studied deposits is summarised in Table 4. Biotite proved to be too weathered for reliable major element analysis by EPMA. Magnetite and ilmenite pairs occur as free crystals in the matrix and also as inclusions within orthopyroxene and, to a lesser extent, amphibole. Fe–Ti oxide pairs included within same host orthopyroxene were targeted to ensure textural equilibrium for use in temperature estimates.

*Kidnappers fall deposit mineral chemistry*

Plagioclase compositions from the Kidnappers fall deposit range from $An_{68}$ to $An_{24}$ and $Or_{0.8}$ to $Or_{4.8}$ (Fig. 12a). Plagioclase core compositions show considerable overlap, even from horizons where KF-A or KF-B material separately dominate (Tables 1 and 5), and range over $An_{64–28}$ and $Or_{3.90–0.85}$. Plagioclase rim values, however, cover only ~10 mol.% An, compared with a ~30 mol.% range for cores at each stratigraphic height (Fig. 12a). Minimum plagioclase rim values change with stratigraphic height from ~$An_{35}$ at the base to ~$An_{26}$ at the

top of the deposit (Fig. 12a). Plagioclase rim compositions throughout the deposit display a bimodal distribution at $An_{32.5}$ $Or_{3.75}$ and $An_{37.5}$ $Or_{2.75}$ (Supplementary Fig. 3), although where the KF-A glass is dominant only the $An_{37.5}$ $Or_{2.75}$ mode occurs, with KF-A glass selvedges (Cooper *et al.*, 2012). Broader ranges and bimodal distributions in major and trace element compositions of rims are found in samples where glass types KF-B and KF-C are also present as shards (Supplementary Fig. 3). The lower An (and Mg) plagioclase mode at $An_{32.5}$ $Or_{3.75}$ (Fig. 13) is therefore associated with the dominant KF-B glass but there is no specific plagioclase composition that can be definitively linked to KF-C glass (Cooper *et al.*, 2012). Core-to-rim variations in Ba (increase) and Mg (decrease) are associated with plagioclase from the KF-B group, whereas grains from the KF-A group have no core-to-rim compositional shifts (Fig. 13).

Orthopyroxene compositions range between $En_{65–42}$ and $Wo_{5.6–1.2}$ (Fig. 12b). The majority of cores are between ~$En_{43–50}$ and $Wo_{1.75–3.50}$ with a scatter to $En_{65}$ and $Wo_{1.2–5.6}$ (Fig. 14). Orthopyroxene cores from horizons where KF-A and KF-B glass compositions separately dominate show considerable compositional overlap, with a bimodal distribution at ~$Wo_{2.2}$ and ~$Wo_{2.5}$ (Supplementary Fig. 4). Grains from horizons where the KF-B glass dominates show a unimodal distribution defining a peak at $Wo_{2.5}$. Orthopyroxene rims, in general, show a tight compositional range between ~$En_{42–48}$ and $Wo_{1.6–3.0}$ (Fig. 14), but also have a bimodal distribution with peaks at $Wo_{2.2}$ and $Wo_{1.8}$ (Supplementary Fig. 4). A significant core-to-rim drop in Ca ($Wo_{2.5–1.8}$) is displayed in ~40% of grains from KF-B-dominated horizons (Supplementary Fig. 4). Significant core-to-rim shifts in chemistry, in contrast, are absent in grains from horizons where KF-A glass dominates. Orthopyroxenes from the KF-A-dominant horizons have a more restricted range in trace element concentrations and, in general, slightly higher Co (50–57 ppm) than in other fall samples where more than one glass group occurs (Fig. 14).

Amphibole rims and the majority of cores (251 analyses) plot in the field of magnesiohornblendes: of the other cores, 14 are tschermakitic pargasites and 4 are magnesiohastingsites (terminology of Leake *et al.,* 2004). Amphibole core and intermediate domain compositions cover the whole of the compositional range ($Al^T$ 1–2) but rims have a smaller range ($Al^T$ 1.05–1.62). Average core compositions from lower (KF-A glass dominated) and upper (KF-B glass dominated) parts of the fall deposit are very similar (Table 4). No consistent core-to-rim shifts in $Al^T$ are present in any samples, but a number of grains associated with KF-B material show a core-to-rim decrease in $TiO_2$ (Supplementary Fig. 5). When $Al^T$ is plotted against other site-specific cation proportions such as $(Na+K)^A$, a slight inflection in the data array is observed at $Al^T$ ~1.2 (Fig. 15). Inflections are also visible when Mn and Zr are plotted against amphibole Eu/Eu* (total range from 0.7 to 0.2) (Fig. 15), used here as a quantitative measure of the degree of evolution of the host melt (Allan *et al.,* 2013). Cores with Eu/Eu* >0.3 do not show a systematic trend in trace element concentrations, whereas in contrast, cores and rims with Eu/Eu* <0.3 show sharp increases in Mn and decreases in Zr with decreasing Eu/Eu* (Fig. 15).

Magnetite compositions fall in the overall range of $X_{usp0.27–0.46}$ and show a bimodal distribution with respect to $Al_2O_3$. Ilmenite has a compositional range of $X_{ilm0.87–0.93}$ and shows a bimodal distribution with respect to MnO (Cooper *et al.,* 2012).

*Kidnappers ignimbrite pumice mineral chemistry*

Plagioclase cores from pumices in each of the whole-rock compositional groups have similar mean compositions (Table 4). Plagioclase rim compositions cluster into three populations, based on either average or minimum An values, that correspond to the three whole-rock compositional groups (Fig. 12d; Table 4). Plagioclases from KI-3 pumices show core-to-rim increases in An and decreases in Or proportions (Supplementary Fig. 3), reflected in the

dominance (82%) within this group of BSE-light rims (Fig. 10). The opposite is the case for plagioclase from the KI-2 samples. Plagioclase trace elements display parallel patterns to the major elements, with KI-3 grains showing core-to-rim increases in Mg and Sr and a decrease in Ba, the reverse of the trends in KI-1 and KI-2 grains (Fig. 13). Clear differences in Mg, Ba and Sr concentrations are present between KI-3, versus KI-1 and KI-2 plagioclase rims (Fig. 13).

Orthopyroxene compositions range from $En_{68–41}$ and $Wo_{5.2–1.1}$ (Fig. 12e). Each of the pumice compositional groups have very similar mean core compositions, but mean rim compositions vary systematically with the whole-rock and glass compositions (Fig. 14; Table 4). Rim compositions range by ~10 mol.% En within KI-3 pumices, but by only ~5 mol.% within KI-1 and KI-2 pumices (Fig. 12e). A core-to-rim drop in mean CaO of 1.2 to 1.0 wt.% ($Wo_{2.5–2.0}$) is found in crystals within the KI-2 group, whereas ~40% of crystals from the KI-3 group display a rimward rise in Ca (Fig. 14). Crystal rim trace element concentrations typically plot into distinct fields that can be linked to the whole-rock composition of their host pumice (Fig. 14). Rims of grains from KI-1 and KI-2 pumices form parallel trends and discrete groups on a plot of $TiO_2$ versus Y (Fig. 14), with grains from the KI-3 pumices forming an extension of the KI-1 field back to higher concentrations.

Amphibole cores plot in the fields of magnesiohornblende and tschermakite–pargasite and outermost rims are all in the magnesiohornblende field. Total amphibole compositions range from $Al^T$ = 0.99 to 1.94 (Fig. 12f). Amphibole core compositions have a large scatter ($Al^T$ 1.02–1.88) but mean $Al^T$ values are very similar between whole-rock compositional groups (Fig. 11f; Table 4). Rim $Al^T$ values (Table 4), along with other elemental concentrations such as $TiO_2$ (Supplementary Fig. 5), covary with the host pumice compositional group. KI-3 amphiboles show a significant core-to-rim increase in $Al^T$ (1.31-1.42) whereas KI-2 amphiboles show the opposite (1.28-1.15) (Fig. 15; Table 4). $TiO_2$

concentrations in amphibole cores are similar in each group (~1.6 wt.%), but rim compositions are distinct in each group, i.e., ~1.2 (KI-2), ~1.6 (KH-1) and ~2.0 wt.% $TiO_2$ (KH-3) (Supplementary Fig. 5). When $Al^T$ is plotted against other site-specific cation proportions such as $(Na + K)^A$ and $Mg/(Mg + Fe^{3+})$, an inflection in data is observed at $Al^T$ = ~1.2 (Fig. 15). This inflection is more prominent in amphiboles from the ignimbrite pumices than those in the Kidnappers fall deposit and Rocky Hill ignimbrite. A sharp increase in Mn and decrease in Zr concentrations occurs with the change in Eu/Eu* from 0.3 to 0.2 (Fig. 15).

Magnetite (total range of $Usp_{24–51}$) and ilmenite ($Ilm_{87–89}$) occur as inclusions in a high proportion of orthopyroxenes, and to a lesser extent in amphiboles. Magnetites from the KI-3 pumices extend to higher $TiO_2$, and have a mean of $Usp_{35}$, compared to $Usp_{31}$ in the KI-1 and KI-2 pumices, although ilmenite compositions are very similar between groups ($Ilm_{87–89}$) (Table 4).

*Rocky Hill ignimbrite pumice mineral chemistry*

Plagioclase cores have similar mean compositions in RH-1 and RH-2 pumices (Table 4). Mean rim compositions from RH-1 plagioclase are almost identical to their associated cores ($An_{36}$ $Or_{2.4}$), but RH-2 rims show more evolved compositions ($An_{30}$ $Or_{3.3}$; Table 4). The lower An rim compositions correspond to the higher proportion of dark BSE rims within this group (Fig. 11). All core-to-rim trends recorded in grains from RH-1 and RH-2 groups are very similar to trends in plagioclase in the KI-1 and KI-2 pumice groups, respectively (Figs. 11 and 13). RH-2 type grains display core-to-rim decreases in Mg and Sr and increases in Ba, whereas cores from RH-1-type grains have concentrations both higher and lower than their associated rims (Fig. 13). Clear differences in Mg, Ba and Sr concentrations characterise RH-1 and RH-2 rims, corresponding with the discrete An modes (Fig. 13).

Orthopyroxene compositions range from $En_{63–42}$ and $Wo_{4.38–1.46}$ (Fig. 12h). Rim compositions within each pumice range by <5 mol.% En. (Fig. 12h) and rims from the two pumice groups have the same mean En values. Orthopyroxene rims from RH-2 pumices show a tight clustering around $Wo_{1.6}$, compared with $Wo_{2.4}$ in RH-1 grains (Fig. 14; Table 4). A consistent core-to-rim drop in Ca (Wo component) is reflected in the dominance of normal zoned orthopyroxenes within the RH-2 group (Fig. 11). Trace element concentrations in crystal rims from the RH-1 and RH-2 groups fall into distinct clusters, which overlie rim compositions of the KI-1 and KI-2 groups, respectively (Fig. 14). The trend towards higher elemental concentrations observed in crystals from the KI-3 group is not seen in the Rocky Hill crystals (Fig. 14).

Rocky Hill amphiboles are commonly complexly zoned, with cores plotting in the field of magnesiohornblende and tschermakite–pargasite, and rims in the magnesiohornblende field. Core compositions span the total range recorded ($Al^T$ = 0.97–1.99) and mean $Al^T$ values are almost identical between whole-rock groups (Fig. 12i; Table 4). Mean RH-1 rim compositions are similar to associated cores, but have significant lower $Al^T$ values within the RH-2 group (Table 4). RH-1 amphiboles have both cores and rims with modes close to ~1.6 wt.% $TiO_2$, whereas in RH-2 amphiboles the cores (mode ~1.5 wt.%) and rims (mode ~1.2 wt.% $TiO_2$) are different (Supplementary Fig. 5). The core-to-rim trends observed within Rocky Hill amphiboles from the RH-1 and RH-2 pumice groups are, as with other mineral phases, closely similar to those within KI-1 and KI-2 groups, respectively (Supplementary Fig. 5).

Magnetite inclusions within orthopyroxene are in the range of $Usp_{23–50}$ and ilmenite inclusions fall between $Ilm_{80–91}$. Mean magnetite and ilmenite compositions do not vary significantly between pumice compositional groups and are between $Usp_{29–32}$ and $Ilm_{87–88}$ (Table 4).

## Model temperatures and pressures

Here, we present (Table 5) and compare estimates of intensive variables for the Kidnappers and Rocky Hill samples, obtained using amphibole (Ridolfi *et al*., 2010 (R2010, below); Putirka, 2016), Fe–Ti oxides (Ghiorso & Evans, 2008), and plagioclase–melt and orthopyroxene–melt (Putirka, 2008) models.

### *Amphibole model temperature and pressure estimates*

*Kidnappers fall deposit*: Amphibole cores from horizons separately dominated by KF-A and KF-B glass compositions have overlapping ranges in R2010 model temperatures and rims with a total range between 770 and 900 °C (Fig. 16). Amphibole core R2010 model pressures are closely similar in samples from any stratigraphic position in the fall deposit. Rims cover a smaller model pressure range than cores, from 80 to 160 MPa in both KF-A- and KF-B-dominated fall material (Fig. 16).

*Kidnappers ignimbrite*: Amphibole core R2010 model temperatures show little difference between samples, with a peak at 790–800 °C and a tail to ~920 °C (Fig. 16). Rim model temperatures from crystals in both the KI-1 and KI-2 pumice groups have broad peaks between 780–800 °C, similar to associated core temperatures. In contrast, amphiboles from the KI-3 pumice group show core-to-rim temperature increases, with peak rim model temperatures of 810–840 °C. This pattern is reflected in R2010 model pressures, with cores displaying peak pressures of 90–130 MPa and a tail to ~270 MPa (Fig. 16). Rim R2010 model pressures from KI-1 and KI-2 pumice groups are tightly clustered, similar to associated core pressures (80–130 MPa) but without the tail to higher pressures, whereas rim model pressures from the KI-3 group are higher (130–170 MPa) than in their respective cores. The values for

R2010 model temperature and pressure from the KI-1 and KI-2 groups are similar to those in the fall deposit, but the KI-3 samples have a higher temperatures and pressures (Fig. 16).

*Rocky Hill ignimbrite*: Amphibole core R2010 model temperatures are similar between pumice compositional groups, with the majority between 770 and 820 °C and a tail to ~920 °C (Fig. 16). Rim R2010 model temperatures from the RH-1 amphiboles are indistinguishable from those of the cores (both 780–820 °C). In contrast, RH-2 rim temperatures are cooler (760–780 °C) and the core-to-rim decrease (~20 °C) is greater than in the otherwise similar high-$SiO_2$ KI-2 group. R2010 model pressures from cores display a narrow range between 90 and 120 MPa with a minor tail to ~270 MPa (Fig. 16). R2010 model pressures from the rims are similar to those recorded in the cores (RH-1: 90–140 MPa; RH-2: 80–120 MPa) but without the tail to higher pressures.

As a test for validation and consistency, R2010 model temperature and pressure estimates are compared to those of Putirka (2016). The pressure independent model (equation 5 of Putirka, 2016) returns average compositional group core and rim temperatures that are 10-20 °C higher than those of R2010 (Table 5). The amphibole-liquid model (equation 9 of Putirka, 2016) returns average compositional group core and rim temperatures between 10 °C lower and 15 °C higher than those of R2010. The models of Putirka (2016) thus yield the same relative core to rim temperature shifts, and compositional group differences as do the R2010 models (Table 5). In contrast, the average pressures estimated using the Putirka (2016) model (his equation 7a) are significantly higher (290-400 MPa) than those of R2010. Relative core to rim relationships in pressure are not the same as those using R2010 (Table 5). The Putirka (2016) equation 7a model uses liquid compositions (including $H_2O$) in equilibrium with amphibole. Average water concentrations (5.2-5.3 wt. %) for this purpose were independently calculated using the plagioclase hygrometer of Waters & Lange (2015).

As another test for consistency, R2010 model pressure estimates were used in turn to estimate temperatures with the plagioclase–hornblende thermometer of Holland & Blundy (1994). The resulting calculated model temperatures cover a larger range than the Ridolfi *et al.* (2010) temperatures (typically 100 °C range in each pumice), but mean temperatures from each model are within 20 °C of each other. Therefore, amphibole temperature and pressure estimates using Ridolfi *et al.* (2010) appear to be at least internally consistent with temperature estimates using the method of Holland & Blundy (1994).

*Fe–Ti oxide temperature and $fO_2$ estimates*

Magnetite and ilmenite pairs included within the same host orthopyroxene and, but to a lesser extent, amphibole were targeted to ensure textural equilibrium (Blundy *et al.,* 2006). All oxide pairs used passed the equilibrium test of Bacon & Hirschmann (1988).

*Kidnappers fall deposit*: The total suite of estimates shows a bimodal distribution throughout the fall deposit (Fig. 17), and mean values vary between KF-A dominated horizons (810 °C) and KF-B dominated horizons (785 °C) (Table 5). The temperature ranges recorded in samples from horizons dominated by the KF-A and KF-B glass types are similar to the ranges from the KI-1 and KI-2 ignimbrite groups (Fig. 17). Data from all other horizons display bimodality. Log $fO_2$ estimates fall on the NNO buffer curve and cover a range from –11.6 to –15.5 (Fig. 17), whereas mean values vary slightly with stratigraphic height (Table 5).

*Kidnappers ignimbrite*: The oxide pairs show a broader range in model temperatures (760–970 °C) than in the fall deposit. The temperature ranges within each compositional group, and in each individual pumice are larger than the range in amphibole rim model temperatures, but are within the respective uncertainties. Log $fO_2$ estimates fall on the NNO buffer curve and cover a range from –10.8 to –14.9 (Fig. 17), with mean values also varying with compositional group (Table 5).

*Rocky Hill ignimbrite*: Model temperature estimates cover a similar range to the Kidnappers ignimbrite of 750–960 °C and also show variations in mean values with whole-rock group (Fig. 17; Table 5). Temperature and $fO_2$ estimates from RH-1 and RH-2 pumices are very similar to those in the KI-1 and KI-2 groups, respectively.

*Plagioclase–melt and orthopyroxene–melt temperature estimates*

Due to the presence of multiple melt compositions within Mangakino eruptives (Cooper *et al*., 2012), it was considered important to use melt (glass) compositions that are directly associated (within a common pumice) with crystal populations. Only crystal rims were used so as to maximise the likelihood of equilibrium between crystals and melt. Due to the challenges in matching loose crystals to glass shard compositional groups within the Kidnappers fall deposit, plagioclase–melt and orthopyroxene–melt temperatures were estimated from ignimbrite pumices only.

The plagioclase–melt thermometer of Putirka (2008) is strongly sensitive to the $H_2O$ content of the melt, which was estimated for each pumice using the plagioclase hygrometer of Waters & Lange (2015). Average model water contents range from 4.8-6.7 wt. % $H_2O$ in Kidnappers pumice and 5.1-5.9 wt. % $H_2O$ in Rocky Hill pumices. All model water content estimates from amphibole rims using Ridolfi *et al.* (2010) (5.2–5.7 wt.% $H_2O$) are within range of the Waters & Lange (2015) estimates. Putirka (2008) model temperatures from Kidnappers plagioclase range from 745–840 °C (Supplementary Fig. 6), with the mean values from each compositional group being distinctive (KI-1 = 780 °C, KI-2 = 750 °C, KI-3= 820 °C; Table 5). Model temperatures for the Rocky Hill plagioclase are more restricted, and can be grouped into two tight modes representing grains from RH-1 (mean of 785 °C) and RH-2 (mean of 760 °C: Supplementary Fig. 6; Table 5).

Model orthopyroxene–melt temperatures using the methods of Putirka (2008) in the Kidnappers KI-2 group crystals display multiple modes from 720–770 °C (750 °C mean), whereas KI-1 group crystals range between 740 and 800 °C (775 °C mean), and KI-3 group crystals have a broad distribution with a mean of 795 °C (Supplementary Fig. 6). In contrast, 50% of Rocky Hill pumice samples contain orthopyroxene that is not in equilibrium with the melt (using the criteria of Putirka, 2008). For example, two samples of RH-1 (P2029, P2030: Fig. 3) and one of RH-2 (P2046) pumices have significantly lower matrix glass Mg concentrations (Fig. 9) and melt–rim pairs are far from equilibrium. Where crystal rims are in equilibrium with the melt, mean model temperatures are 770 °C in the RH-1 group and 760 °C in the RH-2 group (Supplementary Fig. 6; Table 5).

## DISCUSSION

### Reliability of geothermobarometry estimates

Published uncertainties for the different thermobarometers are large (±22–44 °C; see Table 5), although by using the averages of large datasets, the relative differences (as opposed to absolute values) between calculated temperatures will have smaller uncertainties. Much of the variation in temperature and pressure estimates from the Kidnappers and Rocky Hill samples is within each model uncertainty. The relative differences in model temperatures reported above between pumice compositional groups remain consistent, however, whether the estimates use amphibole, Fe–Ti oxides, plagioclase–melt or orthopyroxene–melt methods. Here we consider some of the disparities in geothermobarometry estimates and their possible causes.

The Al-in-amphibole barometer of Ridolfi *et al*. (2010) is based on simple regression of $Al_{tot}$ from selected experiments at a known pressure and therefore all variability in Al content is expressed as a pressure change. Therefore, in magmatic systems involving multiple,

evolving and interacting melts, changes in the Al concentration of the melt can increase amphibole $Al_{tot}$ values without any accompanying change in pressure (e.g., Coombs *et al.,* 2013; Erdmann *et al.,* 2014; Kiss *et al.,* 2014; Putirka, 2016). However, in New Zealand rhyolites (Allan *et al*., 2012; Cooper & Wilson, 2014; Barker *et al*., 2015), the Ridolfi *et al*. (2010) barometer yields geologically reasonable estimates, consistent with evidence from volatile studies (Dunbar *et al*., 1989; Liu *et al*., 2006) and model estimates using the other mineral phases. Magmas at Mangakino are plagioclase saturated and Al-buffered, and therefore, variations in the Al content of amphibole, which are not interpreted to be the result of mixing on the basis that other compositional parameters do not change, have the potential to be controlled by pressure (although with large uncertainties: Putirka, 2016). There are no significant differences in the Eu/Eu* values in glass and amphiboles from KI-2 and RH-2 pumices to suggest that magma mixing caused the amphibole $Al_{tot}$ trends. Thus the core-to-rim decreases in $Al_{tot}$ in the KH-2 and RH-2 amphiboles are interpreted to reflect changes in pressure. Within the Kidnappers KI-3 group pumices, however, amphiboles record core-to-rim increases in both model temperature (~40 °C) and pressure (~40 MPa; Fig. 16). The former can be explained by an input of hotter, less evolved magma, consistent with core-to-rim compositional changes within the other phases. We thus interpret the rise in model pressures as an artifact of the changes in melt Al concentrations, driving increased amphibole $Al_{tot}$ values.

The average pressures estimated using the Putirka (2016) model (equation 7a) are around three times higher, and relative core to rim relationships in pressure are not coherent when compared to the model pressures of Ridolfi *et al.* (2010). These disparities highlight the difficulties in estimating the pressures of amphiboles at shallow crustal depths and negates the use of interpreting absolute pressure values. The Putirka (2016) model uses global amphibole-liquid experimental data and is water dependent. Therefore amphibole cores, which are likely

not in equilibrium with the matrix glass may well return erroneous values. The Fe-Mg exchange coefficient $K_D(\text{Fe-Mg})^{\text{amph-liq}}$ can be used as a test for amphibole-liquid equilibrium (Putirka, 2016). 75 % of all amphibole analyses from Kidnappers pumice fall outside the suggested range ($K_D$=0.28±0.11) and therefore are not suitable for use with the amphibole-melt models of Putirka (2016).

There is a larger range in Fe–Ti oxide model temperatures from each compositional group when compared with amphibole. This may be a consequence of Fe–Ti oxides responding more rapidly to changes in temperature immediately prior to eruption, over timescales that are too short for the re-equilibration of amphibole compositions (e.g. De Angelis *et al.,* 2013). Alternatively, these differences may reflect the relatively large Fe–Ti oxide model uncertainties (Blundy & Cashman, 2008), coupled with a high number of modeled equilibrium pairs, resulting in a large spread in temperatures.

The ranges in plagioclase–liquid and orthopyroxene–liquid model temperatures are smaller in both eruption deposits when compared to other thermometry techniques. In part this is due to the use of only crystal rims (not cores), but is also an artifact of the thermometry models, which are strongly reliant on melt and $H_2O$ concentrations. The use of average matrix glass values and average modeled $H_2O$ concentrations reduces the number of variables in temperature calculations, thus reducing the range of modeled temperatures.

**Melt evolution processes from amphibole signatures**

Inflections observed within amphibole major- and trace-element data with increasing evolution of the bulk-pumice compositions can be linked to changes affecting the overall melt-dominant bodies (Fig. 15). The sharp drop in $(\text{Na} + \text{K})^{\text{A}}$ with decreasing $\text{Al}^{\text{T}}$ (at ~1.2), particularly evident in KI-2 type rims (Fig. 15), is inferred to reflect continued plagioclase and/or biotite crystallisation (removal of Na + K from the melt). Both Kidnappers and Rocky

Hill amphibole Mg/(Mg + $Fe^{3+}$) and Mn values increase with decreasing $Al^T$ (at <1.2), which is interpreted to reflect orthopyroxene instability (cf. Allan *et al.,* 2013). Inflections in amphibole Mn and Zn concentrations with both Eu/Eu* and model pressures are also consistent with orthopyroxene instability in the more evolved (Eu/Eu* < 0.3), inferred lower (model) pressure melts (Fig. 15). The breakdown of orthopyroxene, preferentially enriched in Mg, Mn and Zn when compared to amphibole (Supplementary data), increases the availability of these elements in the melt. This inference is supported by qualitative differences in orthopyroxene proportions from KI-2 (amph > opx) and KI-3 (opx > amph) group pumices in the Kidnappers ignimbrite. These features are the opposite of those observed in the Oruanui rhyolite, where orthopyroxene was more prevalent at lower pressures in the melt-dominant body (Allan *et al.,* 2013).

Zr concentrations in Kidnappers/Rocky Hill amphiboles show a change also at the same point as Mn does (at Eu/Eu* = 0.3; Fig. 15), in response to the onset of zircon crystallisation and subsequent removal of Zr from the melt. The upward trend in Zr concentrations in a minority of amphibole cores with Eu/Eu* values of 0.8–0.3 suggests the presence of an antecrystic amphibole component which originally grew in zircon-undersaturated conditions. These antecrystic cores may have crystallised at deeper levels and/or pre-date the 1.1 and 1.0 Ma peak crystallisation episodes inferred from U–Pb zircon age spectra (Cooper *et al.*, 2014). We suggest that the amphibole changes at Eu/Eu* < 0.3, model pressures <120 MPa, and depths of 4.5–4.0 km reflect a change in crystal growth in the final zircon saturated, melt-dominant bodies that were erupted. The inflection at Eu/Eu* < 0.3 is particularly evident in the KI-2 and RH-2 compositional groups, which also have a large proportion of 'down temperature' core-to-rim textural and chemical changes, as well as core-to-rim decreases in model amphibole temperature and pressure estimates (Fig. 16). These data are consistent with the idea of a decompression event, representing significant extraction of

melt and crystals from a mush/source zone to establish the KI-2/RH-2 melt-dominant body at shallower levels. The timing of this process cannot be constrained through zircon U–Pb ages as zircon growth within the mush zones versus melt dominant bodies cannot be definitively distinguished. However, within Kidnappers pumices, there are two (low and high aspect ratio) populations of zircons, with the high aspect ratio population representing rapid zircon crystallisation that is, within analytical uncertainty, the same as eruption age (Cooper *et al.*, 2014). Extraction of magma from a mush to establish a melt dominant body has the potential to be geologically rapid (cf. Oruanui: Allan *et al.,* 2013).

**Distinct magma batches at Mangakino**

Glass and whole-rock chemistry, coupled with the textures and chemistry of minerals in both eruption deposits suggest that each distinct compositional group underwent different evolutionary pathways and were held at distinct P–T conditions prior to eruption, consistent with the idea that distinct magma batches were tapped by both eruptions. Even so, the overall similarities of crystal chemistry and textures between the Kidnappers and Rocky Hill samples suggest growth within a common mush system, undergoing the same system-wide processes with the same fractionating assemblages. This source contributed crystals in the assembly of the final erupted melt-dominant bodies for both the Kidnappers and Rocky Hill eruptions. The mush source from which the crystals and melt were derived had a broadly similar composition and is inferred (from model pressure values) to have been lodged at similar or greater depths (~4–10 km) to the eruptible melt-dominant bodies (3.5–6.5 km). The geochemical similarities across all the erupted compositions in both eruptions is in part due to the dominance of greywacke crust within the TVZ, which exerts a strong control on the generation and final composition of TVZ silicic melts (McCulloch *et al.,* 1994; Graham *et al.,* 1995; Price *et al*., 2015). The model depths estimated here from amphiboles are comparable

to those inferred for other large-scale silicic systems (Brown *et al.,* 1998a; Wallace *et al.,* 1999; Bachmann *et al.,* 2002; Liu *et al.,* 2006; Wilson *et al.,* 2006; Hildreth & Wilson, 2007). The general similarities in temperature and pressure estimates also imply that the distinctive melt-dominant bodies tapped throughout the Kidnappers and Rocky Hill eruptions were laterally separated rather than vertically stacked in the crust.

A unique crystal and glass geochemical signature is particularly evident in the KI-3 compositional group that is not found within the earlier erupted Kidnappers fall, or later erupted Rocky Hill deposits. The majority of crystals in all phases from the KI-3 group display reverse zoning; light BSE rims (higher An) in plagioclase (Fig. 10) and dark BSE rims (higher En) in orthopyroxene (Fig. 11). Traversing from core-to-rim, Al increases in all crystal phases studied, particularly amphibole and orthopyroxene (Figs. 14 and 15). These core to rim shifts correspond to an apparent temperature increase of ~40 °C (Fig. 16). This evidence, coupled to the increased range and unique trends in major and trace element glass chemistry within the KI-3 group points towards interaction with a less evolved, Al-rich end-member melt that did not mix to any significant extent with the other pumice compositional groups. The KI-3 glass has no counterpart within the fall deposit implying also that this was a discrete magma batch, only tapped during ignimbrite emplacement. We infer that mafic interaction with the KI-3 magma source explains the chemical and temperature changes within this particular, relatively small-volume, body and has the potential to have 'primed' it for eruption (cf. Matthews *et al.,* 2012). However, apart from the KI-3 group, there is no evidence from crystals from a more mafic magma interacting with the rhyolites forming the rest of the erupted materials, through remobilisation of mush, or eruption triggering.

KI-1 and KI-2 type pumice glasses are similar to (but extend the compositional ranges of) the KF-A (plus KF-C) and KF-B type glass groups in the fall deposit, respectively. Also, the proportions of mineral textures from the fall can be matched to those of the pumice

groups. For example at the base of the fall deposit (KF-A dominant), dark BSE plagioclase rims are only sparsely present (<10%), similar to KI-1 pumices (12%). Similarly, a significant increase in the abundance of dark BSE plagioclase rims (typical of KI-B pumice) coincides with the appearance of KF-B glass. We thus infer that the KI-1 and KF-A, and KI-2 and KF-B group materials originated from the same two melt-dominant bodies and share common magmatic processes as types A and B material of Cooper *et al.* (2012), respectively. During eruption of the fall deposit, more restricted bodies of melt were tapped, and hence less glass heterogeneity is observed (although the fall deposit is ~2/3 of the total eruption volume). After the onset of ignimbrite deposition, more variable (and heterogeneous) melt was tapped from these melt-dominant bodies (cf. Kennedy *et al*., 2008). Overlapping matrix glass compositions in the KI-1 and KI-2 pumice groups suggest that the parental melt-dominant bodies may have undergone some mutual mixing during ignimbrite generation, and not remained separate as they were in the earlier eruption stages. However, the distinctive crystal textural characteristics in the KI-1 and KI-2 groups imply that the two magmas had undergone different crystallisation histories. In general, minerals from KI-1 pumices have no significant core-to-rim changes in textures, chemistry or model P–T estimates, whereas those from KI-2 display normal zoning ('down temperature' signals). We thus infer that the KI-1/KF-A melt-dominant body experienced relatively uniform P–T conditions and similar melt Al concentrations in the lead-up to eruption, whereas the KI-2/KF-B body cooled (core-to-rim decrease in model temperature of ~20–30 °C), with accompanying crystal growth and fractionation. Alternatively, if the amphibole model pressure decrease of ~10 MPa is considered valid, the KI-2/KF-B down-temperature signature may reflect the extraction of material from a deeper mush zone to form a shallower melt-dominant body prior to eruption, as seen in the Oruanui eruption (Allan *et al.*, 2013).

The KF-C glass (Type C of Cooper *et al.,* 2012) is not represented as a discrete compositional field in the Kidnappers ignimbrite (KI-1 matrix glass compositions overlap both KF-A and KF-C glass groups). The KF-C glass type diminishes in abundance upwards in the fall deposit (Cooper *et al.,* 2012), and it is inferred that this melt was either exhausted during fall deposit stages of the activity, or that its remnants were incorporated into the KF-A/KI-1 melt-dominant body.

In the Rocky Hill ignimbrite, crystal textures (Figs. 10, 11) and chemistries (Fig. 12) from the RH-1 and RH-2 groups correspond to those in KI-1 and KI-2, respectively. RH-1 crystals show little core-to-rim changes in chemistry or model P–T estimates and have similar proportions of non-distinct plagioclase rims and unzoned orthopyroxene grains to their KI-1 counterparts. RH-2 crystals are dominated by normal zoning ('down temperature' signals) with decreases in model core-to-rim temperatures (~20–30 °C) and pressures (10 MPa), as in KI-2. We interpret these similarities to suggest that the two main melt-dominant bodies tapped in the Kidnappers were erupted again in the Rocky Hill, or that similar processes re-established two new magma batches within the same source systems. The similarity of zircon U–Pb age spectra from the Rocky Hill and Kidnappers (Cooper *et al.,* 2014) suggest growth within a common system and imply that magmatic processes recorded by Rocky Hill crystals must pre-date the Kidnappers eruption. However, further crystal growth also occurred during the time-break between the eruptions, and a significant proportion of plagioclase-rich crystal mush with associated brown glass was incorporated into the melt dominant body. Also, deposits of the Rocky Hill do not contain any 'KI-3 type' material (either glass compositions or reversely zoned crystals), consistent with the Rocky Hill ignimbrite representing a separate eruption.

There are other examples of large silicic eruptions that discharged multiple melt batches with distinct compositional signatures that cannot easily be related by any

differentiation or fractional crystallisation process within a single magma body (e.g., Fridrich & Mahood, 1987; Schuraytz *et al.,* 1989; Briggs *et al.,* 1993; Cambray *et al.,* 1995; Mills *et al.,* 1997). Most of these studies propose models whereby the discrete melt batches are held within a single unitary magma chamber, with barriers required to inhibit mixing between compositional groups (e.g., Cambray *et al.,* 1995; Mills *et al.,* 1997). Such a scenario, however, requires highly complex withdrawal dynamics and arbitrary barriers to mixing, and may be reconsidered in view of the Kidnappers/Rocky Hill system. In this system, the compositional separation is more simply accomplished by having horizontally separated melt-dominant bodies. Such features have previously been documented in the TVZ (Gravley *et al.,* 2007; Shane et al., 2007, 2008a, 2008b; Bégué et al., 2014), although for volumes mostly two orders of magnitude smaller than these examples.

**Volumes of the magma types**

The relative sizes of magma bodies represented by each compositional group can be inferred to a first order through the proportions of pumices collected for analysis. On the basis of whole-rock data, 3 of 42 Kidnappers ignimbrite pumices belong to the KI-3 compositional group, suggesting that this group comprises <10% of the total juvenile material. The KI-3 group is not represented in the Kidnappers fall deposit (i.e., ~2/3 of the total erupted extra-caldera material) and this distinctive magma batch therefore represents <3% of the erupted magma overall. The KI-1 group is the dominant composition within the Kidnappers ignimbrite (27 out of 42 pumices: ~65 %), with the KI-2 group making up the remaining ~30%. These volume proportions of KI-1 and KI-2 are broadly similar to the proportions of KF-A (~68%) and KF-B (~22%) glass material reported from the fall deposit (Cooper *et al*., 2012). If we infer that these respective groups in the fall and flow originated from common melt-dominant bodies (KF-A = KI-A; KF-B = KI-B) then total contributions of erupted

magma from the two largest melt-dominant bodies are ~65% (780 $km^3$ DRE) and ~25% (300 $km^3$ DRE), respectively. The two other less voluminous melts, KI-3 and KF-C are ~3% (40 $km^3$ DRE) and ~7% (80 $km^3$ DRE). These absolute estimates may be ±50% (cf. Hildreth, 1981, his Fig. 1), but the relative proportions are unlikely to change. The respective magma volumes discharged in the Rocky Hill eruption are less well constrained due to the continuous range in whole-rock compositions making a clear distinction between RH-1 and RH-2 difficult. On the basis of glass chemistry proportions, however, the RH-1 group (linked to KI-1 and KF-A) remains the dominant magma type.

**Compositional and mineralogical comparisons between products of the Kidnappers and Rocky Hill eruptions**

As a whole, glasses from the Kidnappers and Rocky Hill eruptions are unusual in the fact that both major and trace element chemical heterogeneity is displayed over a complete range of scales, from chamber-wide, through single-clast, to sub-millimetre scales. Although some rhyolitic eruptions in the TVZ have compositional variations in glass (e.g. Nairn *et al*., 2004; Shane *et al.,* 2003, 2008b), this level of heterogeneity is unusual in most TVZ rhyolitic eruptions (e.g. Sutton *et al.,* 1995; Allan *et al.,* 2008). The switch from fall activity to ignimbrite generation in the Kidnappers eruption is inferred to have been accompanied by wider scale caldera collapse, which disrupted the systematic withdrawal of discrete magma bodies (Cooper *et al*., 2012), and triggered the catastrophic evacuation of all magma batches.

The pumice glasses from the Kidnappers and Rocky Hill ignimbrites provide evidence for contrasting magmatic processes involved in each eruption. $K_2O$ concentrations in Kidnappers pumices (particularly KI-2) are greater than would be expected from fractional crystallisation of the minerals present, and whole-rock to glass $K_2O$ tie-lines have negative slopes (Fig. 4) indicating the addition of $K_2O$. Magma mixing can be ruled out as a cause of

$K_2O$ addition as respective glass $K_2O$ concentrations are not elevated and do not show larger variations. The $K_2O$ addition is better explained by incorporation of xenocrystic biotite into Kidnappers magmas (Fig. 4), consistent also with higher Rb concentrations, and increasing Rb/Sr ratios in Kidnappers whole-rock data, although the latter is also influenced by the plagioclase content of the pumices (Fig. 5).

In contrast to the Kidnappers, whole-rock to glass $K_2O$ tie-lines within Rocky Hill pumices have positive slopes (Fig. 7) consistent with a fractional crystallisation trend. Whole-rock $Al_2O_3$ values extend to considerably higher concentrations in Rocky Hill pumices than in the Kidnappers with little accompanying change in glass values (Fig. 7), consistent with a greater abundance of Al-rich phases (plagioclase and amphibole). Whole-rock Y concentrations in the Kidnappers samples do not correlate with $Al_2O_3$, whereas in the Rocky Hill they form a tightly defined trend (Fig. 8). Y is particularly enriched in amphibole ($[Y_{amph}]/[Y_{melt}] = 10$) when compared to the other major crystal phases (supplementary electronic appendices). The Rocky Hill data thus imply that there was either a strong amphibole crystallisation control or an input of amphibole into the melt dominant bodies during the time gap between the Kidnappers and Rocky Hill eruptions.

Major element matrix glass compositions in Rocky Hill pumices have smaller ranges than those within Kidnappers pumices (Fig. 9), while trace element concentrations have a larger range within the RH-1 group in comparison to KI-1. The reduction in major element diversity in the pumices is inferred to reflect convective stirring in the chamber in the aftermath of Kidnappers caldera collapse (e.g., Marshall & Sparks, 1984; Folch *et al.,* 2001; Kennedy & Stix, 2007; Kennedy *et al.,* 2008). An alternative, but not opposing possibility is that smaller and compositionally more uniform sources were tapped during the Rocky Hill eruption, as suggested by the narrower range in model temperature and pressure estimates. Rim compositions within the Rocky Hill crystals also plot into tighter and more discrete

groups, reflecting a reduction in the compositional diversity of the melt. The two glass compositional groupings within the Rocky Hill are remarkably similar to the KF-A and KF-B Kidnappers fall deposit glass compositional groups. If we infer that the RH-1 and RH-2 melt groups originated from the same sources as the KF-A/KI-1 and KF-B/KI-2 melt groups, then there are two possible end-member scenarios.

First, portions of the two distinctive melt-dominant bodies remained after the Kidnappers eruption and were re-erupted. This scenario alone is precluded by the differences in crystal zonation patterns and the differences in glass types between the two suites of deposits. In particular, there is the brown glass selvedges and thick bubble walls associated with plagioclase-bearing clots and 'phenoclasts', commonly found within Rocky Hill pumices but exceedingly rare within Kidnappers pumices. This brown glass has fluid-affected compositions (low $K_2O$, Rb and Li; high $Na_2O$: Supplementary Fig. 1), typically infilling and surrounding shattered plagioclase grains. The brown glass phenoclasts are contained within pumice with 'normal' glass chemistry and therefore this alteration is not secondary or a result of vapour-phase alteration in the deposit during cooling. We interpret these clots and associated glass to represent the incorporation of a disrupted plagioclase-rich border zone to the magma body. In addition, $Al_2O_3$ values in the Rocky Hill pumices are significantly higher at the same Eu/Eu* values as the Kidnappers pumices/glasses and do not trend towards their respective glass compositions (Figs. 4 and 7). Also, the whole-rock compositional array does not trend toward its respective glass compositions (Fig. 7), implying that an additional plagioclase component is present in Rocky Hill pumices, consistent with the addition of antecrystic material from a crystal mush.

Second, two melt-dominant bodies were re-established anew during the time break between the two events, incorporating new material from common deeper mush sources and replicating the earlier voluminous KI-1 and KI-2 magma bodies. This scenario alone is

precluded by our interpretation of the closely similar zircon age characteristics between the Kidnappers and Rocky Hill samples (Cooper *et al*., 2014). If the Rocky Hill melt-dominant bodies were wholly newly created, then we would expect a greater proportion of the zircons to have come from the inherited 1.1 Ma crystallization mode. We thus interpret the Rocky Hill crystals and melts forming magma types RH-1 and RH-2 to represent a combination of new material extracted from a common crystal mush with existing remnants of the two largest melt dominant bodies tapped during the Kidnappers eruption.

**A model of the magmatic system for the Kidnappers and Rocky Hill eruptions**

The following outlines the evolution of the Kidnappers/Rocky Hill magmatic system illustrated in Fig. 18, from eruption of the Kidnappers fall deposit and to the Rocky Hill eruption.

*Earlier Kidnappers eruption (fall deposits)*

During the eruption of the Kidnappers fall deposit, three discrete, horizontally separated melt-dominant bodies (type KF-A, KF-B and KF-C) are inferred to have been tapped from three vent systems to yield the simultaneous and sequential compositional changes in the fall deposit (Cooper *et al.,* 2012) (Fig. 18). No interaction or mixing took place between the melt-dominant bodies during this stage. The erupted volumes of melt were homogeneous, with little or no evidence for stratification and were stored at depths of ~3.5 to 6.5 km. The systematic tapping of the three horizontally separated melt-dominant bodies may have been controlled by tectonic processes following the partial drainage of the magma body feeding glass group KF-A and its associated crystals (Cooper *et al.,* 2012). Due to the volumes of magma that were evacuated during this stage, it seems likely that caldera collapse accompanied the eruption of the Kidnappers fall deposit. The initial caldera collapse may

have been related to geographically separated vents (cf. Gravley *et al.,* 2007), and therefore deposition of the fall deposit remained systematic, rather than being accompanied by gross mixing of the glass types.

*Later Kidnappers eruption (ignimbrite)*

Draining of the melt-dominant bodies and tectonic readjustment is inferred to have caused further and more widespread caldera collapse and a consequent increase in the eruption intensity to generate the pyroclastic flows that deposited the Kidnappers ignimbrite. We suggest that tectonic rupturing may have occurred between the initially separated calderas, leading to wider scale collapse and an increase in the eruption intensity driving the fall-to-flow transition. It is inferred that the ignimbrite-forming stage saw the evacuation of a wider diversity of material from three distinct batches of melt plus crystals (Fig. 18). The earlier KF-C melt dominant body was either incorporated into the volumetrically dominant KF-A/KI-1 magma body, or had been entirely drained during the earlier fall deposit stage of the eruption.

Of the two major magma bodies, material erupted from the KF-A/KI-1 magma body had remained at a uniform depths and without any significant changed in temperature prior to eruption, as represented in the mineral zonations. In contrast KF-B/KI-2 magma body rose to shallower depths and experienced a fall in temperatures shortly before eruption. We interpret this to represent the extraction of large volumes of crystals and melt from a deeper crystal mush to establish a melt-dominant body at shallower levels. The KI-2 pumices also contain more biotite, suggesting a greater involvement of lower temperature, biotite-richer marginal material at shallower levels, represented in whole-rock and glass compositional trends. The somewhat smaller KI-3 magma body interacted with hotter, lesser evolved melts during pre-

eruptive storage, and did not mix syn-eruptively with the two larger melt-dominant bodies discussed above (Fig. 18).

Each compositional group within the Kidnappers ignimbrite is represented at the same single stratigraphic level where there were no signs of any significant time breaks (e.g. flow unit boundaries). We thus infer that the evacuation of the diverse magmas involved in the later stages of the Kidnappers eruption was simultaneous.

*Prior to and during the Rocky Hill eruption*

Data presented here suggest that in the time break between the Kidnappers and Rocky Hill eruptions, the two largest melt-dominant magma bodies from the Kidnappers eruption were in part reestablished from the same mush regions (Fig. 18). The Rocky Hill melt-dominant bodies were more homogeneous than their counterparts in the Kidnappers, which may reflect: (1) smaller volumes being tapped in the Rocky Hill eruption (2) a significant volume of new melt plus an inherited population of zircons (Cooper *et al.*, 2014) being generated or extracted from the mush/source zone (3) post-Kidnappers caldera collapse and tectonic readjustment stirring magma remaining from the Kidnappers event (Marshall & Sparks, 1984; Folch *et al.,* 2001; Kennedy *et al.,* 2008). The reestablished bodies were more crystal rich (10-20%), which may in part be due to the draining of significant proportions of eruptible melt and the dredging of crystals (particularly plagioclase) from the inferred common mush zone.

It is conceivable that caldera collapse or tectonic readjustments accompanying eruption of the Kidnappers fall deposit may have itself been the trigger mechanism for the firstly systematic, and then repeated evacuation of magma through the Kidnappers and Rocky Hill eruptions (cf. Gravley *et al.,* 2007; Bégué *et al*., 2014). Allan *et al*. (2013) suggested that rifting and extensional processes in the mush-bearing crust prior to the Oruanui eruption promoted melt channels, whereby melt (and crystals) could be extracted to establish the melt-

dominant body over geologically rapid timescales (centuries). A similar scenario is suggested in this system to explain the rapid renewal of eruptible melt and crystals from a common mush zone following the Kidnappers and prior to the Rocky Hill eruption. The evidence from modern Taupo (Sutton *et al*., 1995; Wilson & Charlier, 2009; Allan *et al*., 2012; Barker *et al*., 2015), as well as from Mangakino suggests that parallel magma systems are able to operate in the crust within the conditions of the TVZ.

## CONCLUSIONS

The Mangakino volcanic centre was highly active around 1 Ma, producing ~1200 $km^3$ of magma in the Kidnappers event followed by another ~200 $km^3$ during the Rocky Hill event. From the petrological and geochemical dataset presented here, we conclude the following.

(1) Both field constraints and the general similarity of crystal compositions and textures, glass chemistry and zircon age spectra (Cooper *et al*., 2014) between both eruptions provides unequivocal evidence that magmas for both eruptions came from a common deeper mush system. This system represented a source of crystals (and melt) with broadly similar chemistries giving rise to the compositional similarity of the Kidnappers fall deposit and subsequent Kidnappers and Rocky Hill ignimbrites.

(2) Subtle variations in pumice mineralogy and whole-rock compositions, glass chemistry and crystal textures are consistent with the notion that the Kidnappers and Rocky Hill are distinct events and not the products of one zoned eruption. The renewal of compositionally similar melt-dominant bodies between the Kidnappers and Rocky Hill events, and the geologically short timescales involved highlights the rapidity of the rejuvenation processes at Mangakino.

(3) The systematically zoned Kidnappers fall deposit provides evidence for the tapping of three discrete magma bodies whereas the Kidnappers ignimbrite is more

compositionally diverse. The change from fall to flow is inferred to mark a change in the scale and siting of caldera collapse and the simultaneous evacuation of discrete but compositionally diverse melts. Compositional heterogeneity within the Kidnappers and Rocky Hill ignimbrites is found both at the chamber-wide and pumice scale, and the full compositional spectrum can be found in pumices sampled at any one stratigraphic level within each ignimbrite. Evacuation of a single stratified magma chamber is not a viable option for the Kidnappers/Rocky Hill eruptions. The magmatic system involved multiple melt-dominant bodies, which were apparently drained during the Kidnappers event. The two largest bodies were reestablished from a common source region or mush prior to re-eruption during the Rocky Hill event.

(4) Apart from the KI-3 magma type, there is no evidence to suggest there was interaction with a lesser evolved, hotter magma. Within KI-3, this interaction may have played a role in priming the smaller volume of magma prior to the Kidnappers eruption. However, crystals from the two volumetrically dominant magma types in the Kidnappers and Rocky Hill show no evidence for a temperature increase in the erupted magma, rebomilisation of the mush, or an eruption trigger.

(5) Caldera collapse episodes apparently exerted significant control on the intensity and timing of eruptions at Mangakino. During eruption of the Kidnappers fall deposit, the systematic tapping of discrete magmas suggests that any caldera collapse areas remained separate and confined to an association with each single melt-dominant body (Fig. 18). The change in the Kidnappers eruption from fall deposition to the onset of pyroclastic flows marks an apparent change in the scale and siting of caldera collapse. The rapid rejuvenation of more homogeneous melt-dominant bodies and the triggering of the Rocky Hill eruption, may also be attributed to stirring after caldera collapse and/or a strong extensional tectonic control at Mangakino. Regional rifting processes

may have contributed towards allowing extracted melts and crystals to ascend rapidly to reestablish or renew the melt-dominant bodies on such a short time scale of decades.

**FUNDING**

This work was supported by a Victoria University PhD Scholarship (GFC), and by the Royal Society of New Zealand through the Marsden Fund (VUW0813) and a James Cook Fellowship (CJNW).

**ACKNOWLEDGEMENTS**

We thank Roger Briggs, Michelle Coombs and John Gamble for constructive comments and edits of a preliminary version of this manuscript, Wim Degruyter and Matt Coble for comments on the submitted manuscript and Richard Price for editorial handling.

**SUPPLEMENTARY DATA**

Supplementary data are available at *Journal of Petrology* online

**REFERENCES**

Allan, A. S. R., Baker, J. A., Carter, L. & Wysoczanski, R. J. (2008). Reconstructing the Quaternary evolution of the world's most active silicic volcanic system: insights from an ~1.65 Ma deep ocean tephra record sourced from Taupo Volcanic Zone, New Zealand. *Quaternary Science Reviews* **27**, 2341-2360.

Allan, A. S. R., Wilson, C. J. N., Millet, M. -A. & Wysoczanski, R. J. (2012). The invisible hand: tectonic triggering and modulation of a rhyolitic supereruption. *Geology* **40**, 563-566.

Allan, A. S. R., Morgan, D. J., Wilson, C. J. N. & Millet, M. -A. (2013). From mush to eruption in centuries: assembly of the super-sized Oruanui magma body. *Contributions to Mineralogy and Petrology* **166**, 143-164.

Alloway, B. V., Pillans, B. J., Carter, L., Naish, T. R. & Westgate, J. A. (2005). Onshore-offshore correlation of Pleistocene rhyolitic eruptions from New Zealand: implications for TVZ eruptive history and paleoenvironmental construction. *Quaternary Science Reviews* **24**, 1601-1622.

Bachmann, O. & Bergantz, G. W. (2008). Deciphering magma chamber dynamics from styles of compositional zoning in large silicic ash flow sheets. *Reviews in Mineralogy and Geochemistry* **69**, 651-674.

Bachmann, O., Dungan, M. A. & Lipman, P. W. (2002). The Fish Canyon magma body, San Juan volcanic field, Colorado: rejuvenation and eruption of an upper-crustal batholith. *Journal of Petrology* **43**, 1469-1503.

Bacon, C. R. & Hirschmann, M. M. (1988). Mg/Mn partitioning as a test for equilibrium between coexisting Fe–Ti oxides. *American Mineralogist* **73**, 57-61.

Barker, S. J., Wilson, C. J. N., Allan, A. S. R. & Schipper, C. I. (2015). Fine-scale temporal recovery, reconstruction and evolution of a post-supereruption magmatic system. *Contributions to Mineralogy and Petrology* **170**, article 5.

Bégué, F., Deering, C. D., Gravley, D. M., Kennedy, B. M., Chambefort, I., Gualda, G. A. R. & Bachmann, O. (2014). Extraction, storage and eruption of multiple isolated magma batches in the paired Mamaku and Ohakuri eruption, Taupo Volcanic Zone, New Zealand. *Journal of Petrology* **55**, 1653-1684.

Best, M. G. & Christiansen, E. H. (1997). Origin of broken phenocrysts in ash-flow tuffs. *Geological Society of America Bulletin* **109**, 63-73.

Black, T. M. (1992). Chronology of the Middle Pleistocene Kidnappers Group, New Zealand

and correlation to global oxygen isotope stratigraphy. *Earth and Planetary Science Letters* **109**, 573-584.

Blank, H. R. (1965). Ash-flow deposits of the central King Country, New Zealand. *New Zealand Journal of Geology and Geophysics* **8**, 588-607.

Blundy, J. & Cashman, K. (2008) Petrological reconstruction of magmatic system variables and processes. In: Putirka, K. D. & Tepley, F. J. (Eds.), *Minerals, inclusions and volcanic processes*. *Reviews in Mineralogy and Geochemistry* **69**, 179–239

Blundy, J., Cashman, K. & Humphreys, M. (2006). Magma heating by decompression-driven crystallization beneath andesite volcanoes. *Nature* **443**, 76-80.

Briggs, R. M., Gifford, M. G., Moyle, A. R., Taylor, S. R., Norman, M. D., Houghton, B. F. & Wilson, C. J. N. (1993). Geochemical zoning and eruptive mixing in ignimbrites from Mangakino volcano, Taupo Volcanic Zone, New Zealand. *Journal of Volcanology and Geothermal Research* **56**, 175-203.

Brown, S. J. A., Wilson, C. J. N., Cole, J. W. & Wooden, J. (1998a). The Whakamaru group ignimbrites, Taupo Volcanic Zone, New Zealand: evidence for reverse tapping of a zoned silicic magma system. *Journal of Volcanology and Geothermal Research* **84,** 1-37.

Brown, S. J. A., Burt, R. M., Cole, J. W., Krippner, S. J. P., Price, R. C. & Cartwright, I. (1998b). Plutonic lithics in ignimbrites of Taupo Volcanic Zone, New Zealand: sources and conditions of crystallisation. *Chemical Geology* **148**, 21-41.

Cambray, F. W., Vogel, T. A. & Mills, J. G. (1995). Origin of compositional heterogeneities in tuffs of the Timber Mountain Group: the relationship between magma batches and magma transfer and emplacement in an extensional environment. *Journal of Geophysical Research* **100**, 15793-15805.

Carter, L., Alloway, B. V., Shane, P. & Westgate, J. A. (2004). Deep-ocean record of major

late Cenozoic rhyolitic eruptions from New Zealand. *New Zealand Journal of Geology and Geophysics* **47**, 481-500.

Cashman, K. V. & Giordano, G. (2014). Calderas and magma reservoirs. *Journal of Volcanology and Geothermal Research* **288**, 28-45.

Cathey, H. E. & Nash, B.P. (2004). The Cougar Point Tuff: implications for thermochemical zonation and longevity of high-temperature, large volume silicic magmas of the Miocene Yellowstone hotspot. *Journal of Petrology* **45**, 27-58.

Chamberlain, K. J., Wilson, C. J. N., Wallace, P. J. & Millet, M. -A. (2015). Micro-analytical perspectives on the Bishop Tuff and its magma chamber. *Journal of Petrology* **56**, 605-640.

Chesner, C. A. (2012). The Toba caldera complex. *Quaternary International* **258**, 5-18.

Cole, J. W. & Lewis, K. B. (1981). Evolution of the Taupo-Hikurangi subduction system. *Tectonophysics* **72**, 1-21.

Cole, J. W., Milner, D. M. & Spinks, K. D. (2005). Calderas and caldera structures: a review. *Earth-Science Reviews* **69**, 1-26.

Coombs, M. L., Sisson, T. W., Bleick, H. A., Henton, S. M., Nye, C. J., Payne, A. L., Cameron, C. E., Larsen, J. F., Wallace, K. L. & Bull, K. F. (2013). Andesites of the 2009 eruption of Redoubt Volcano, Alaska, *Journal of Volcanology and Geothermal Research* **259**, 349–372.

Cooper, G. F. & Wilson, C. J. N. (2014). Development, mobilization and eruption of a large crystal rich ignimbrite: the Ongatiti ignimbrite, New Zealand. *Lithos* **198-199**, 38-57.

Cooper, G. F., Wilson, C. J. N., Millet, M. -A., Baker, J. & Smith, E. G. C. (2012). Systematic tapping of independent magma chambers during the 1 Ma Kidnappers supereruption. *Earth and Planetary Science Letters* **213-214**, 23-33.

Cooper, G. F., Wilson, C. J. N., Charlier B. L. A., Wooden, J. L. & Ireland, T. R. (2014).

Temporal evolution and compositional signatures of two supervolcanic systems recorded in zircons from Mangakino volcanic centre, New Zealand. *Contributions to Mineralogy and Petrology* **167**, 1018.

De Angelis, S. H., Larsen, J. & Coombs, M. (2013). Pre eruptive magmatic conditions at Augustine volcano, Alaska, 2006: evidence from amphibole geochemistry and textures. *Journal of Petrology* **54**, 1939-1961.

Dunbar, N. W., Hervig, R. L. & Kyle, P. R. (1989). Determination of pre-eruptive $H_2O$, F and Cl contents of silicic magmas using melt inclusions: examples from Taupo volcanic centre, New Zealand. *Bulletin of Volcanology* **51**, 177-184.

Erdmann, S., Martel, C., Pichavant, M. & Kushnir, K. (2014). Amphibole as an archivist of magmatic crystallization conditions: problems, potential, and implications for inferring magma storage prior to the paroxysmal 2010 eruption of Mount Merapi, Indonesia. *Contributions to Mineralogy and Petrology* **167**, article 1016.

Fridrich, C. J. & Mahood, G. A. (1987). Compositional layers in the zoned magma chamber of the Grizzly Peak Tuff. *Geology* **15**, 299-303.

Folch, A., Codina, R. & Martí, J. (2001). Numerical modeling of magma withdrawal during explosive caldera-forming eruptions. *Journal of Geophysical Research* **106**, 16163-16175.

Ghiorso, M. S. & Evans, B. W. (2008). Thermodynamics of rhombohedral oxide solid solutions and a revision of the Fe–Ti two-oxide geothermometer and oxygen-barometer. *American Journal of Science* **308**, 957-1039.

Girard, G. & Stix, J. (2010). Rapid extraction of discrete magma batches from a large differentiating magma chamber: the Central Plateau Member rhyolites, Yellowstone caldera, Wyoming. *Contributions to Mineralogy and Petrology* **160**, 441-465.

Graham, I. J., Cole, J. W., Briggs, R. M., Gamble, J. A. & Smith, I. E. M. (1995). Petrology

and petrogenesis of volcanic rocks from the Taupo Volcanic Zone: a review. *Journal of Volcanology and Geothermal Research* **68**, 59-87.

Gravley, D. M., Wilson, C. J. N., Leonard, G. S. & Cole, J. W. (2007). Double trouble: paired ignimbrite eruptions and collateral subsidence in the Taupo Volcanic Zone, New Zealand. *Geological Society of America Bulletin* **119**, 18-30.

Hildreth, W. (1979). The Bishop Tuff: evidence for the origin of compositional zonation in silicic magma chambers. In: Chapin, C. E. & Elston, W. E. (Eds.) *Ash-flow tuffs*. *Geological Society of America, Special Paper* **180**, 43-75.

Hildreth, W. (1981). Gradients in silicic magma chambers: implications for lithospheric magmatism. *Journal of Geophysical Research* **86**, 10153-10192.

Hildreth, W. (2004). Volcanological perspectives on Long Valley, Mammoth Mountain, and Mono Craters: several contiguous but discrete systems. *Journal of Volcanology and Geothermal Research* **136**, 169-198.

Hildreth, W. & Wilson, C. J. N. (2007). Compositional zoning of the Bishop Tuff. *Journal of Petrology* **48**, 951-999.

Holland, T. & Blundy, J. (1994). Non-ideal interactions in calcic amphiboles and their bearing on amphibole-plagioclase thermometry. *Contributions to Mineralogy and Petrology* **116**, 433-447.

Houghton, B. F., Wilson, C. J. N., McWilliams, M. O., Lanphere, M. A., Weaver, S. D., Briggs, R. M. & Pringle, M. S. (1995). Chronology and dynamics of a large silicic magmatic system: central Taupo Volcanic Zone, New Zealand. *Geology* **23**, 13-16.

Kennedy, B. M. & Stix, J. (2007). Magmatic processes associated with caldera collapse at Ossipee ring dyke, New Hampshire. *Geological Society of America Bulletin* **119**, 3-17.

Kennedy, B. M., Jellinek, A. M. & Stix, J. (2008). Coupled caldera subsidence and stirring inferred from analogue models. *Nature Geoscience* **1**, 385-389.

Kennedy, B. M., Wilcock, J. & Stix, J. (2012). Caldera resurgence during magma replenishment and rejuvenation at Valles and Lake City calderas. *Bulletin of Volcanology* **74**, 833-847.

Kiss, B., Harang, S., Ntaflos, T., Mason, P. R. D. & Pál-Molnár, E. (2014). Amphibole perspective to unravel pre-eruptive processes and conditions in volcanic plumbing systems beneath intermediate arc volcanoes: a case study from Ciomadul volcano (SE Carpathians). *Contributions to Mineralogy and Petrology* **167**, article 986.

Leake, B. E., Woolley, A. R., Birch, W. D., Burke, E. A., Ferraris, G., Grice, J. D., Hawthorne, F. C., Kisch, H.J., Krivovichev, V. G. & Schumacher, J. C. (2004). Nomenclature of amphiboles: additions and revisions to the International Mineralogical Association's amphibole nomenclature. *American Mineralogist* **89**, 883-887

Liu, Y., Anderson, A. T., Wilson, C. J. N., Davis, A. M. & Steele, I. M. (2006). Mixing and differentiation in the Oruanui rhyolitic magma, Taupo, New Zealand: evidence from volatiles and trace elements in melt inclusions. *Contributions to Mineralogy and Petrology* **151**, 71-87.

Lowe, D. J. (2011). Tephrochronology and its application: a review. *Quaternary Geochronology* **6**, 107–153.

Marshall, L. A. & Sparks, R. S. J. (1984). Origin of some mixed-magma and net-veined ring intrusions. *Journal of the Geological Society*, *London* **141**, 171-182.

Martin, R. C. (1961). Stratigraphy and structural outline of the Taupo Volcanic Zone. *New Zealand Journal of Geology and Geophysics* **4**, 449-478.

Matthews, N. E., Huber, C., Pyle, D. M. & Smith, V. C. (2012). Timescales of magma recharge and reactivation of large silicic systems from Ti diffusion in quartz. *Journal of Petrology* **53**, 1385-1416.

McCulloch, M. T., Kyser, T. K., Woodhead, J. & Kinsley, L. (1994). Pb-Sr-Nd-O isotopic constraints on the origin of rhyolites from the Taupo Volcanic Zone of New Zealand: evidence for assimilation followed by fractionation from basalt. *Contributions to Mineralogy and Petrology* **115**, 303-312.

Metz, J. M. & Mahood, G. A. (1985). Precursors to the Bishop Tuff eruption: Glass Mountain, Long Valley, California. *Journal of Geophysical Research* **90**, 11121-11126.

Metz, J. M. & Mahood, G. A. (1991). Development of the Long Valley, California, magma chamber recorded in precaldera rhyolite lavas of Glass Mountain. *Contributions to Mineralogy and Petrology* **106**, 379-397.

Moyle, A. R. (1989). Volcanic geology and geochemistry of the Rocky Hill Ignimbrite, Upper Waipa Valley. M.Sc. thesis University of Waikato, Hamilton, New Zealand.

Miller, C. F. & Wark, D. A. (2008). Supervolcanoes and their explosive supereruptions. *Elements* **4**, 11-16.

Milner, D. M., Cole, J. W. & Wood, C. P. (2003). Mamaku Ignimbrite: a caldera-forming ignimbrite erupted from a compositionally zoned magma chamber in Taupo Volcanic Zone, New Zealand. *Journal of Volcanology and Geothermal Research* **122**, 243-264.

Mills, J. G., Saltoun, B. W. & Vogel, T. A. (1997). Magma batches in the Timber Mountain magmatic system, southwestern Nevada volcanic field, Nevada, USA. *Journal of Volcanology and Geothermal Research* **78**, 185-208.

Nairn, I. A., Shane, P. R., Cole, J. W., Leonard, G. J., Self, S. & Pearson, N. (2004). Rhyolite magma processes of the ~AD 1315 Kaharoa eruption episode, Tarawera volcano, New Zealand. *Journal of Volcanology and Geothermal Research* **131**, 265-294.

Nelson, S. T. & Montana, A. (1992). Sieve-textured plagioclase in volcanic rocks produced by rapid decompression. *American Mineralogist* **77**, 1242-1249.

Ninkovich, D. (1968). Pleistocene volcanic eruptions in New Zealand recorded in deep-sea sediments. *Earth and Planetary Science Letters* **4**, 89-102.

Perkins, M. E. & Nash, W. P. (2002). Explosive silicic volcanism of the Yellowstone hotspot: the ash fall tuff record. *Geological Society of America Bulletin* **114**, 367-381.

Price, R. C., Mortimer, N., Smith, I. E. M. & Maas, R. (2015). Whole-rock geochemical reference data for Torlesse and Waipapa terranes, North Island, New Zealand. *New Zealand Journal of Geology and Geophysics* **58**, 213-228.

Pritchard, C. J. & Larson, P. B. (2012). Genesis of the post-caldera eastern Upper Basin Member rhyolites, Yellowstone, WY: from volcanic stratigraphy, geochemistry and radiogenic isotope modeling. *Contributions to Mineralogy and Petrology* **164**, 205-228

Putirka, K. D. (2008). Thermometers and barometers for volcanic systems. *Reviews in Mineralogy and Geochemistry* **69**, 61-120.

Putirka, K. (2016). Amphibole thermometers and barometers for igneous systems, and some implications for eruption mechanisms of felsic magmas at arc volcanoes. *American Mineralogist* **101**, (in press: doi:10.2138/am-2016-5506).

Ridolfi, F., Renzulli, A. & Puerini, M. (2010). Stability and chemical equilibrium of amphibole in calc-alkaline magmas: an overview, new thermobarometric formulations and application to subduction-related volcanoes. *Contributions to Mineralogy and Petrology* **160**, 45-66.

Rogan, A. M. (1982). A geophysical study of the Taupo Volcanic Zone, New Zealand. *Journal of Geophysical Research* **87**, 4073-4088.

Rotella, M. D., Wilson, C. J. N., Barker, S. J., Schipper, C. I., Wright, I. C. & Wysoczanski, R. J. (2015). Dynamics of deep submarine silicic explosive eruptions in the Kermadec arc, as reflected in pumice vesicularity textures. *Journal of Volcanology and*

*Geothermal Research* **301**, 314-332.

Schuraytz, B. C., Vogel, T. A. & Younker, L. W. (1989). Evidence for dynamic withdrawal from a layered magma body: the Topopah Spring Tuff, southwestern Nevada. *Journal of Geophysical Research* **94**, 5925-5942.

Self, S., Goff, F., Gardner, J. N., Wright, J. V. & Kite, W. M. (1986). Explosive rhyolitic volcanism in the Jemez Mountains: vent locations, caldera development and relation to regional structure. *Journal of Geophysical Research* **91**, 1779-1798.

Shane, P. A. R. (1994). A widespread, early Pleistocene tephra (Potaka tephra, 1 Ma) in New Zealand: character, distribution, and implications. *New Zealand Journal of Geology and Geophysics* **37**, 25-35.

Shane, P., Smith, V. C., Lowe, D. J. & Nairn, I. A. (2003). Re-identification of c. 15 700 cal yr BP tephra bed at Kaipo Bog, eastern North Island: implications for dispersal of Rotorua and Puketarata tephra beds. *New Zealand Journal of Geology and Geophysics* **46**, 591-596.

Shane, P., Martin, S. B., Smith, V. C., Beggs, K. F., Darragh, M. B., Cole, J. W. & Nairn, I. A. (2007). Multiple rhyolite magmas and basalt injection in the 17.7 ka Rerewhakaaitu eruption episode from Tarawera volcanic complex, New Zealand. *Journal of Volcanology and Geothermal Research* **164**, 1-26.

Shane, P., Nairn, I. A., Smith, V. C., Darragh, M., Beggs, K., & Cole, J. W. (2008a). Silicic recharge of multiple rhyolite magmas by basaltic intrusion during the 22.6 ka Okareka eruption episode, New Zealand. *Lithos* **103**, 527–549.

Shane, P., Nairn, I. A., Martin, S. B. & Smith, V. C. (2008b). Compositional heterogeneity in tephra deposits resulting from the eruption of multiple magma bodies: implications for tephrochronology. *Quaternary International* **178**, 44-53.

Simon, J. & Reid, M. R. (2005). The pace of rhyolite differentiation and storage in an

'archetypical' silicic magma system, Long Valley, California. *Earth and Planetary Science Letters* **235**, 123-140.

Singer, B. S. (2014). A Quaternary geomagnetic instability time scale. *Quaternary Geochronology* **21**, 29-52.

Smith, R. L. (1979). Ash-flow magmatism. In: Chapin, C. E. & Elston, W. E. (Eds.) *Ash-flow tuffs*. *Geological Society of America Special Paper* **180**, 5-27.

Smith, R. L. & Bailey, R. A. (1966). The Bandelier Tuff: a study of ash-flow eruption cycles from zoned magma chambers. *Bulletin Volcanologique* **29**, 83-103.

Sparks, R. S. J., Sigurdsson, H. & Wilson, L. (1977). Magma mixing: a mechanism for triggering acid explosive eruptions. *Nature* **267**, 315-318.

Stern, T. A. (1979). Regional and residual gravity fields, central North Island, New Zealand. *New Zealand Journal of Geology and Geophysics* **22**, 479-485.

Stix, J., Goff, F., Gorton, M. P., Heiken, G. & Garcia, S. R. (1988). Restoration of compositional zonation in the Bandelier silicic magma chamber between two caldera-forming eruptions: geochemistry and origin of the Cerro Toledo Rhyolite, Jemez Mountains, New Mexico. *Journal of Geophysical Research* **93**, 6129-6147.

Sutton, A., Blake, S. & Wilson, C. J. N. (1995). An outline geochemistry of rhyolite eruptives from Taupo volcanic centre, New Zealand. *Journal of Volcanology and Geothermal Research* **68**, 153-175.

Tanaka, H., Turner, G. M., Houghton, B. F., Tachibana, T., Kono, M., McWilliams, M. O. (1996). Palaeomagnetism and chronology of the central Taupo Volcanic Zone, New Zealand. *Geophysics Journal International* **124**, 919-934.

Tsuchiyama, A. (1985). Dissolution kinetics of plagioclase in the melt of the system diopside-albite-anorthite, and origin of dusty plagioclase in andesites. *Contributions to Mineralogy and Petrology* **89**, 1-16.

Turner, E. P. (1928). A brief account of the re-establishment of vegetation on Tarawera Mountain since the eruption of 1886. *Transactions of the New Zealand Institute* **59**, 60-66.

Waters, L. E. & Lange, R. A. (2015). An updated calibration of the plagioclase-liquid hygrometer-thermometer applicable to basalts through rhyolites. *American Mineralogist* **100**, 2172-2184.

Watts, K. E., Bindeman, I. N. & Schmitt, A. K. (2012). Crystal scale anatomy of a dying supervolcano: an isotope and geochronology study of individual phenocrysts from voluminous rhyolites of the Yellowstone caldera. *Contributions to Mineralogy and Petrology* **164**, 45-67.

Wilson, C. J. N. (1986). Reconnaissance stratigraphy and volcanology of ignimbrites from Mangakino volcano. In: Smith, I. E. M. (Ed.) *Late Cenozoic Volcanism in New Zealand*. *Royal Society of New Zealand Bulletin* **23**, 179-193.

Wilson, C. J. N. (1993). Stratigraphy, chronology, styles and dynamics of late Quaternary eruptions from Taupo volcano, New Zealand. *Philosophical Transactions of the Royal Society of London* A**343**, 205-306.

Wilson, C. J. N. & Charlier, B. L. A. (2009). Rapid rates of magma generation at contemporaneous magma systems, Taupo volcano, New Zealand: insights from U-Th model-age spectra in zircons. *Journal of Petrology* **50**, 875-907.

Wilson, C. J. N., Rogan, A. M., Smith, I. E. M., Northey, D. J., Nairn, I. A. & Houghton, B. F. (1984). Caldera volcanoes of the Taupo Volcanic Zone, New Zealand. *Journal of Geophysical Research* **89**, 8463-8484.

Wilson, C. J. N., Houghton, B. F., Kamp, P. J. J. & McWilliams, M. O. (1995a). An exceptionally widespread ignimbrite with implications for pyroclastic flow emplacement. *Nature* **378**, 605-607.

Wilson, C. J. N., Houghton, B. F., McWilliams, M. O., Lanphere, M. A., Weaver, S. D. & Briggs, R. M. (1995b). Volcanic and structural evolution of Taupo Volcanic Zone, New Zealand: a review. *Journal of Volcanology and Geothermal Research* **68**, 1-28.

Wilson, C. J. N., Blake, S., Charlier, B. L. A. & Sutton, A. N. (2006). The 26.5 ka Oruanui eruption, Taupo volcano, New Zealand: development, characteristics and evacuation of a large rhyolitic magma body. *Journal of Petrology* **47**, 35-69

Wilson, C. J. N., Charlier, B. L. A, Fagan, C. J., Spinks, K. D., Gravley, D. M., Simmons, S. F. & Browne, P. R. L. (2008). U-Pb dating of zircon in hydrothermally altered rocks as a correlation tool: application to the Mangakino geothermal field, New Zealand. *Journal of Volcanology and Geothermal Research* **176**, 191-198

Wilson, C. J. N., Gravley, D. M., Leonard, G. S. & Rowland, J. V. (2009). Volcanism in the central Taupo Volcanic Zone, New Zealand: tempo styles and controls. In: Thordarson, T., Self, S., Larsen, G., Rowland, S. K. & Hoskuldsson, A. (Eds.), *Studies in Volcanology: The Legacy of George Walker*. *Special Publications of IAVCEI* **2**, 225-247.

Wolff, J. A., Ramos, F. C. & Davidson, J. P. (1999). Sr isotope disequilibrium during differentiation of the Bandelier Tuff: constraints on the crystallization of a large rhyolitic magma chamber. *Geology* **27**, 495-498.

Wolff, J. A., Brunstad, K. A. & Gardner, J. N. (2011). Reconstruction of the most recent volcanic eruptions from the Valles caldera, New Mexico. *Journal of Volcanology and Geothermal Research* **199**, 53-68.

## Figure Captions

**Fig. 1.** Map of the North Island, New Zealand showing the extent of the Kidnappers and Rocky Hill ignimbrites and sampling locations. The thick dashed line marks the boundary of the old TVZ. Modified from Briggs *et al.* (1993) and Wilson *et al.* (1995b).

**Fig. 2.** Images to show the typical field relationships of the Kidnappers and Rocky Hill deposits. (a) Contrasts between the natural exposures of the Rocky Hill ignimbrite and the temporary or artificial exposures of the Kidnappers deposits. Road cutting is at 38.562259°S, 175.417357°E. (b) Exposure in a road cutting at 38.567042°S, 175.464727°E that shows the erosional nature of the contact between the Kidnappers and Rocky Hill ignimbrites.

**Fig. 3.** Diagrammatic catalogue of samples from the Kidnappers fall deposit, Kidnappers ignimbrite and Rocky Hill ignimbrite chosen for crystal-specific studies and glass analyses. Kidnappers fall samples are ordered in stratigraphic height through the proximal fall deposit. Pumice from the ignimbrites are arranged by whole-rock compositional groups ($SiO_2$ wt.%) and are without stratigraphic control. The colours assigned to compositional groups are used in all figures throughout this paper. Note that the stratigraphic heights covered by the term 'other' (light blue) contain material from KF-C, as well KF-A and KF-B fall deposit compositional groups. Major element analyses are indicated with a 'm', and trace element analyses are denoted by a 't'.

**Fig. 4.** Plots of whole-rock (circles) and matrix glass (triangles) major oxide abundances against silica for all analysed Kidnappers single pumice clasts. Tie-lines connect whole-rock–glass pairs. Crosses represent whole-rock 2 sd XRF uncertainties (left hand side) and 2 sd EPMA matrix glass uncertainties (right hand side) (Electronic

Appendix 1). Colours of the symbols indicate the compositional groups assigned to each pumice (KI-1 = red, KI-2 = green, KI-3 = blue; Fig. 3). Mineral accumulation vectors are shown to highlight influence of the variable crystal content on pumice whole-rock concentrations (p=plagioclase, a=amphibole, o=opx, b=biotite).

**Fig. 5**. Plots of selected trace elements versus silica (a–c), $K_2O$ (d) and $Al_2O_3$ (e, f) for pumice whole-rock and matrix glass from Kidnappers pumice. Tie-lines connect whole-rock–glass pairs. Crosses represent 2 sd whole-rock solution ICPMS uncertainties (Electronic Appendix 1). Colours of the symbols indicate the compositional groups assigned to each pumice (KI-1 = red, KI-2 = green, KI-3 = blue; Fig. 3).

**Fig. 6.** Selected major and trace element plots of Kidnappers matrix glass. Each data point represents a single matrix glass analysis. Spots are divided into three groups based on whole-rock compositional groups (KI-1, KI-2 and KI-3; Fig. 3), and shaded areas highlight the compositional range covered by the glass compositional groups in the Kidnappers fall deposit identified in Cooper *et al*. (2012) (KF-A = red, KF-B = green, KF-C = light blue (KF-C contains KF-C glass and variable proportions of KF-A and KF-B; see Cooper *et al*., 2012 and Fig. 3).

**Fig. 7.** Plots of whole-rock (diamonds) and matrix glass (triangles) major element abundances against silica for all analysed Rocky Hill single pumice clasts. Tie-lines connect whole-rock–glass pairs. The range of Kidnappers data is shown by the coloured areas (KI-1 = red, KI-2 = green, KI-3 = blue; Fig. 3) for whole-rock analyses and grey areas (glass analyses). Crosses represent whole-rock 2 sd XRF uncertainties (left hand side) and 2 sd EPMA matrix glass uncertainties (right hand side) (Electronic Appendix 1).

**Fig. 8.** Plots of selected trace elements versus silica (a–c), $K_2O$ (d) and $Al_2O_3$ (e,f) for pumice whole-rock and matrix glass from Rocky Hill pumices. Tie-lines connect whole-rock–glass pairs. Crosses represent 2 sd whole-rock solution ICPMS uncertainties (Electronic Appendix 1). Colours of the symbols indicate the compositional groups to which pumices are assigned (RH-1 = red, RH-2 = green; Fig. 3).

**Fig. 9.** Plots of selected major and trace elements of Rocky Hill matrix glass. Each data point represents a single matrix glass analysis. Spots are divided into two groups based on whole-rock compositional groups. Coloured shaded areas represent the corresponding ranges covered by matrix glass compositional groups within Kidnappers pumice (KI-1 = red, KI-2 = green, KI-3 = blue; Fig. 3).

**Fig. 10.** Summary of textural features (based on BSE imaging) of Kidnappers and Rocky Hill plagioclase grains from each pumice compositional group. Plagioclase grains are divided into three populations based on the BSE intensity change from intermediate domains to outermost rims. 'Light rims' and 'dark rims' are grains that have prominent outermost rims that are either lighter or darker than their interior domains. 'Non-distinct rims' do not show a significant change in brightness from their associated interior domains.

**Fig. 11.** Summary of textural features (based on BSE imaging) of Kidnappers and Rocky Hill orthopyroxene grains from each pumice compositional group. Normally zoned orthopyroxenes are those with darker (higher En) cores and lighter (lower En) outer zones. Nominally unzoned grains do not show any significant compositional zonation, although some streaky discontinuous zoning may be present. Reversely zoned grains have lighter (lower En) cores and darker (higher En) outer zones. Patchy grains display a range of compositions but zoning is

discontinuous and no core–rim relationships are observed. Bar charts show the proportions of grain populations within each compositional group. A dark exterior zone (e) may be superimposed on any of the four textures, and the proportions of grains with dark exteriors (as a percentage of total orthopyroxene grains) are shown.

**Fig. 12.** Summary plots of mineral composition for plagioclase, orthopyroxene and amphibole from the Kidnappers fall deposit (a–c) versus stratigraphic height in the fall deposit where sampled (Fig. 3), Kidnappers ignimbrite (d–f) and Rocky Hill ignimbrite (g–i) versus the compositions of their host pumices. Dashed lines mark divisions between glass compositional groups in the Kidnappers fall deposit and pumice compositional groups within the Kidnappers and Rocky Hill ignimbrites.

**Fig. 13.** In situ Or (mol.%) and trace element compositions versus An (mol.%) of plagioclase from the Kidnappers fall deposit (a–c), Kidnappers ignimbrite (d–f) and Rocky Hill ignimbrite (g–i).

**Fig. 14.** In situ major and trace element compositions of orthopyroxenes from the Kidnappers fall (a–c), Kidnappers ignimbrite (d–f) and Rocky Hill ignimbrite (g–i).

**Fig. 15.** In situ major and trace element compositions of amphiboles from the Kidnappers fall deposit (a–c), Kidnappers ignimbrite (d–f) and Rocky Hill ignimbrite (g–i). Approximate position of inflection points discussed in the text are marked with dashed lines.

**Fig. 16.** Stacked histograms of amphibole core and rim apparent temperatures (°C) and pressures (MPa) from each compositional group within Kidnappers and Rocky Hill pumices and horizons where the KF-A and KF-B glass compositional groups

dominate the material within the fall deposit (Fig. 3). Apparent amphibole temperatures and pressures were calculated using the method of Ridolfi *et al*. (2010).

**Fig. 17.** Fe–Ti oxide model temperatures and oxygen fugacities calculated using the methods of Ghiorso & Evans (2008). Apparent temperatures from all Fe–Ti oxide equilibrium pairs in each compositional group are displayed as stacked histograms. Calculated oxygen fugacity values ($\log fO_2$) vs. temperature (°C) from each compositional group are shown.

**Fig. 18.** Semi-quantitative cross sections of the Kidnappers/Rocky Hill magmatic systems through time. (1) During the early stages of the Kidnappers eruption, material was erupted from at least two independent magma chambers (plus the possible minor KF-C magma) as a phreatomagmatic fall (Cooper *et al*., 2012). Caldera collapse probably commenced during the fall phase. (2) Eruption and deposition of material deposited as flows was coincidental with wholescale caldera collapse. During this period, a wider range of compositions were tapped from two, heterogeneous melt-dominant bodies which had little exchange of crystals or melt. A third smaller volume of melt underwent late-stage heating and mixing with a more primitive, mafic melt, but did not mix with the other Kidnappers magmas. (3) After a short time break the Rocky Hill eruption commenced. Two smaller homogeneous melt-dominant bodies, broadly similar to Type A and B of the early Kidnappers were tapped. Collapse of the chamber roof and margins incorporated altered material into the melt (

red arrows). Depths are estimated from amphiboles using the method of Ridolfi *et al*. (2010). The horizontal extents in (1) are approximately estimated from the volume of

erupted material and the general size of the gravity anomaly that defines the Mangakino caldera.

**Supplementary Fig. 1.** $K_2O$ versus Rb for Rocky Hill matrix glass and brown glass from a single pumice clast. (a) BSE image of a broken plagioclase grain with associated brown glass between fragments and surrounding grain. (b) Photograph of a pumice chip to show the textural relationship between matrix glass and brown glass, which is found in association with crystal clots.

**Supplementary Fig. 2.** Summary of textural features of plagioclase and orthopyroxene grains from samples through the Kidnappers fall deposit (Cooper *et al.*, 2012). These textures are discussed in the text with representative images and the proportions in the ignimbrite pumices in Figs 10 and 11.

**Supplementary Fig. 3.** Stacked histograms to summarise the compositional (An mol.%) relationships between plagioclase cores and rims from the each compositional group in the Kidnappers fall deposit, Kidnappers ignimbrite and Rocky Hill ignimbrite. Colour designations for each compositional group are the same as in Fig. 3 in the main paper.

**Supplementary Fig. 4.** Stacked histograms to summarise the compositional (Wo mol.%) relationship between orthopyroxene cores and rims from the Kidnappers fall deposit, Kidnappers ignimbrite and Rocky Hill ignimbrite. Colour designations are as in Fig. 3 in the main paper.

**Supplementary Fig. 5.** Stacked histograms to summarise the compositional relationships between amphibole cores and rims from the Kidnappers fall deposit, Kidnappers ignimbrite and Rocky Hill ignimbrite. Colour designations are as in Fig. 3 in the main paper.

**Supplementary Fig. 6.** Stacked histograms of plagioclase–liquid and orthopyroxene–liquid model temperatures from each compositional group within just the Kidnappers and Rocky Hill pumices. Apparent temperatures were calculated using the

methods of Putirka (2008). Temperatures were calculated using only the rims of plagioclase and orthopyroxene grains, with matrix glass compositions from the same pumice clast.

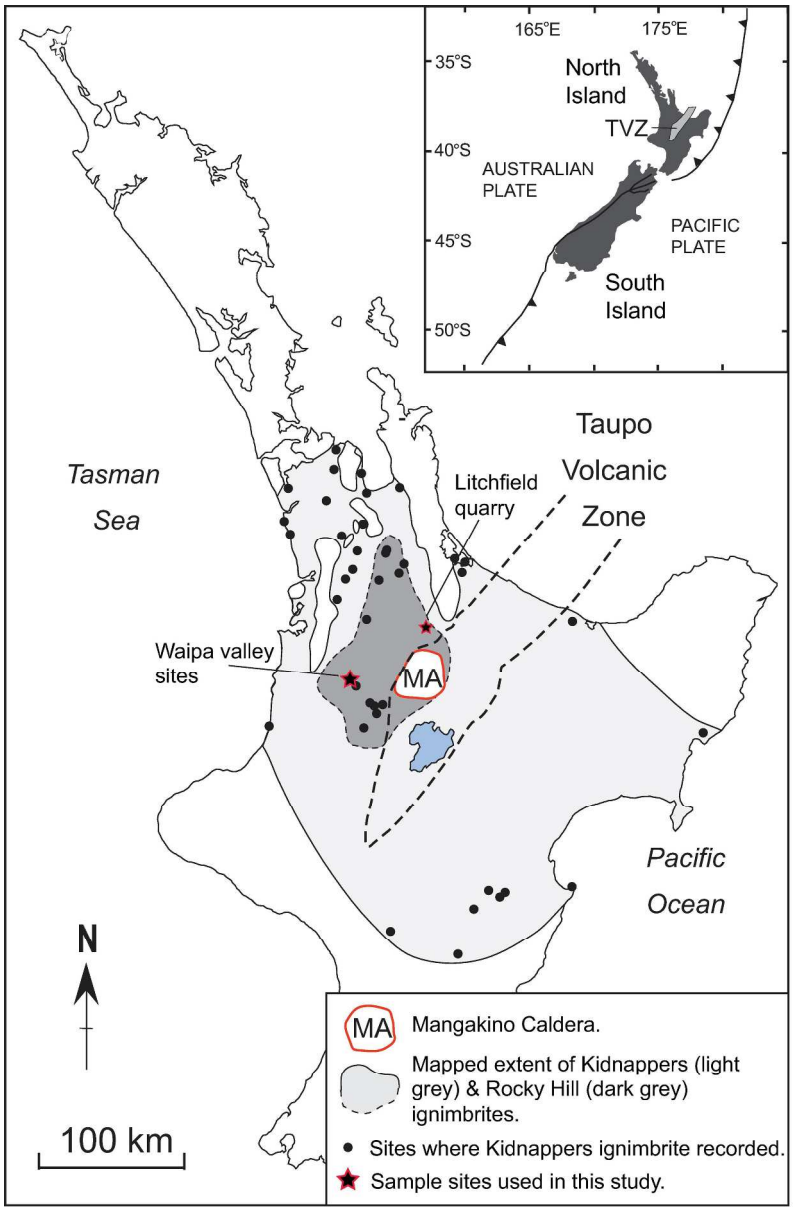


Fig.1
210x315mm (300 x 300 DPI)

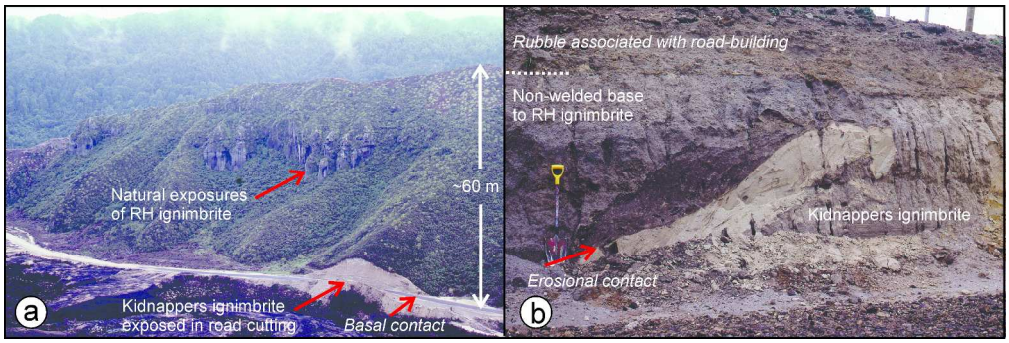


Fig. 2
334x110mm (300 x 300 DPI)

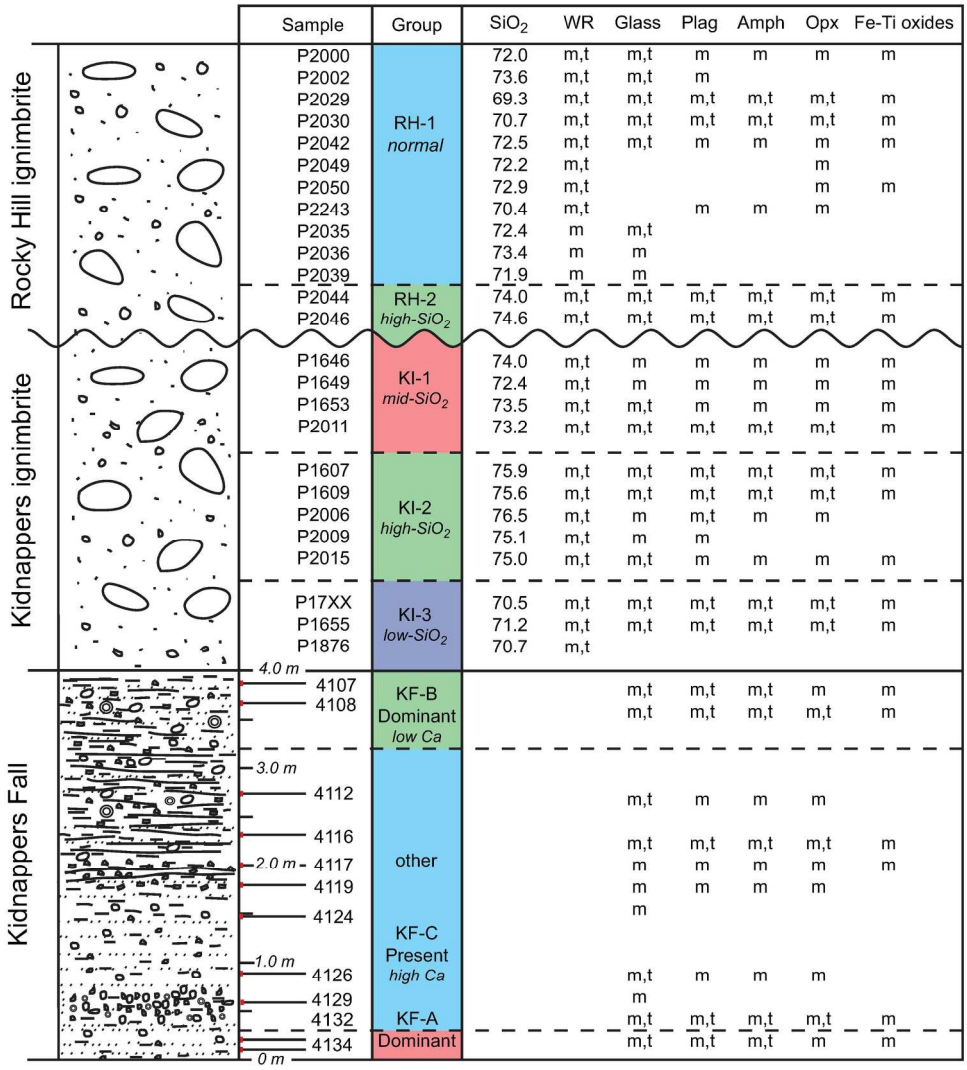


| Sample | Group | $SiO_2$ | WR | Glass | Plag | Amph | Opx | Fe-Ti oxides |
|---|---|---|---|---|---|---|---|---|
| P2000 | RH-1 *normal* | 72.0 | m,t | m,t | m | m | m | m |
| P2002 | | 73.6 | m,t | m,t | m | | | |
| P2029 | | 69.3 | m,t | m,t | m,t | m,t | m,t | m |
| P2030 | | 70.7 | m,t | m,t | m,t | m,t | m,t | m |
| P2042 | | 72.5 | m,t | m,t | m | m | m | m |
| P2049 | | 72.2 | m,t | | | | m | |
| P2050 | | 72.9 | m,t | | | | m | m |
| P2243 | | 70.4 | m,t | | m | m | m | |
| P2035 | | 72.4 | m | m,t | | | | |
| P2036 | | 73.4 | m | m | | | | |
| P2039 | | 71.9 | m | m | | | | |
| P2044 | RH-2 *high-$SiO_2$* | 74.0 | m,t | m,t | m,t | m,t | m,t | m |
| P2046 | | 74.6 | m,t | m,t | m,t | m,t | m,t | m |
| P1646 | KI-1 *mid-$SiO_2$* | 74.0 | m,t | m | m | m | m | m |
| P1649 | | 72.4 | m,t | m | m | m | m | m |
| P1653 | | 73.5 | m,t | m,t | m | m | m | m |
| P2011 | | 73.2 | m,t | m,t | m,t | m,t | m,t | m |
| P1607 | KI-2 *high-$SiO_2$* | 75.9 | m,t | m,t | m,t | m,t | m,t | m |
| P1609 | | 75.6 | m,t | m,t | m,t | m,t | m,t | m |
| P2006 | | 76.5 | m,t | m | m,t | m | m | |
| P2009 | | 75.1 | m,t | m | m | | | |
| P2015 | | 75.0 | m,t | m,t | m | m | m | m |
| P17XX | KI-3 *low-$SiO_2$* | 70.5 | m,t | m,t | m,t | m,t | m,t | m |
| P1655 | | 71.2 | m,t | m,t | m,t | m,t | m,t | m |
| P1876 | | 70.7 | m,t | | | | | |
| 4107 | KF-B Dominant *low Ca* | | | m,t | m,t | m,t | m | m |
| 4108 | | | | m,t | m,t | m,t | m,t | m |
| 4112 | other | | | m,t | m | m | m | |
| 4116 | | | | m,t | m,t | m,t | m,t | m |
| 4117 | | | | m | m | m | m | m |
| 4119 | | | | m | m | m | m | |
| 4124 | | | | m | | | | |
| 4126 | KF-C Present *high Ca* | | | m,t | m | m | m | |
| 4129 | | | | m | | | | |
| 4132 | KF-A Dominant | | | m,t | m,t | m,t | m,t | m |
| 4134 | | | | m,t | m,t | m,t | m | m |

Fig. 3
192x236mm (300 x 300 DPI)

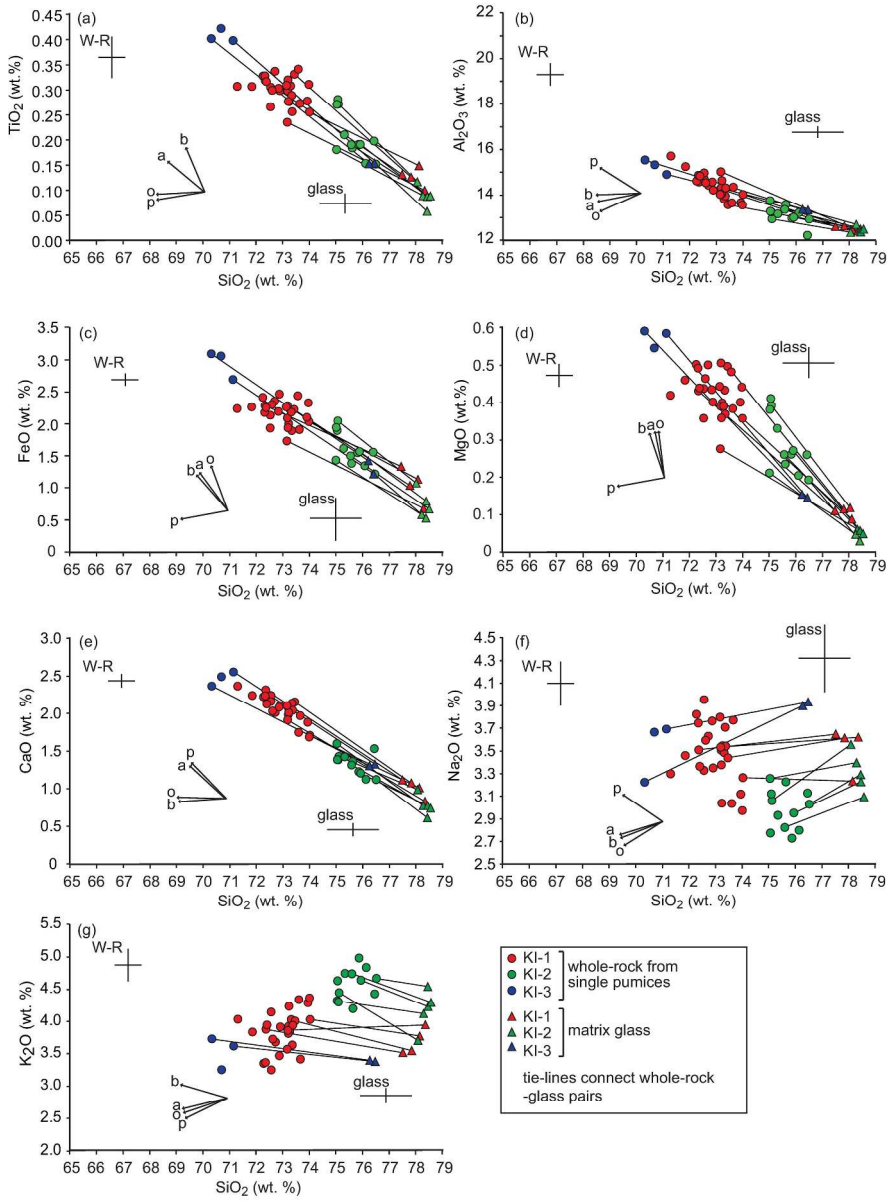


Fig. 4
272x326mm (300 x 300 DPI)

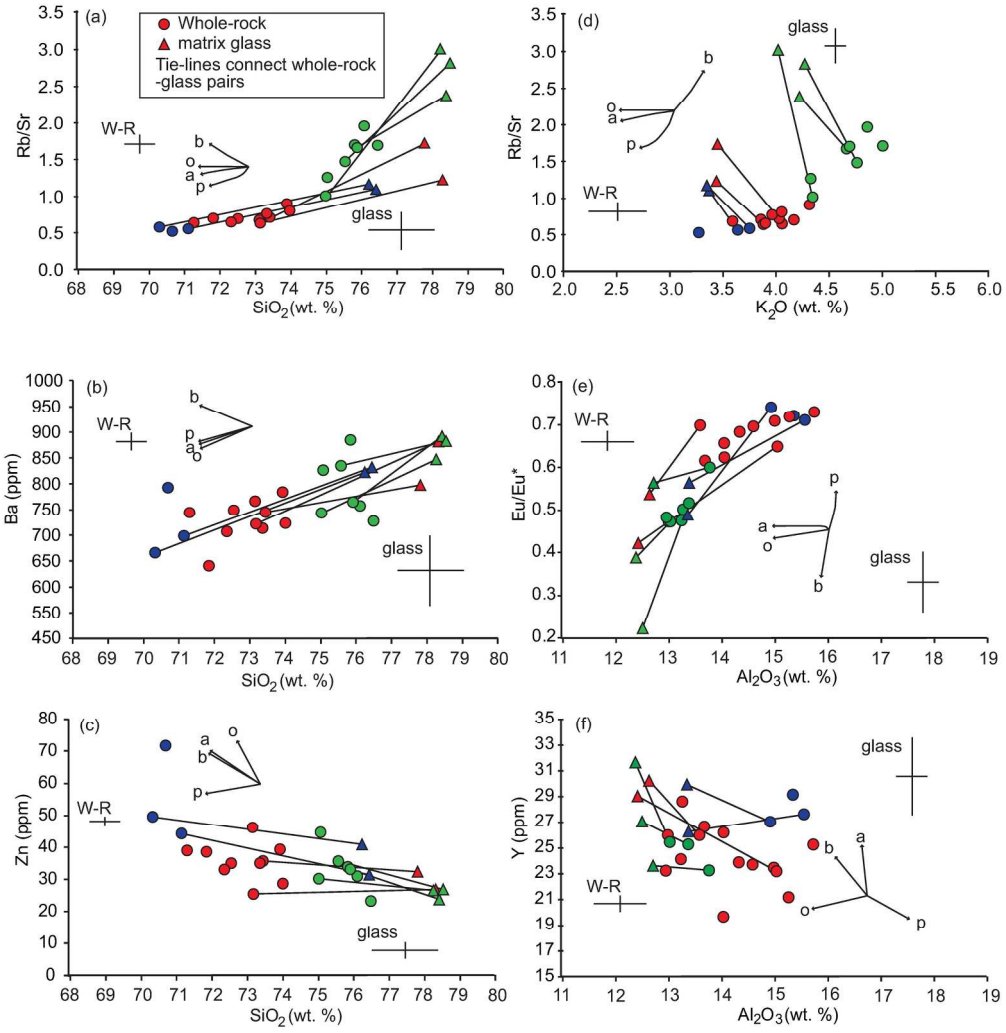


Fig. 5
208x215mm (300 x 300 DPI)

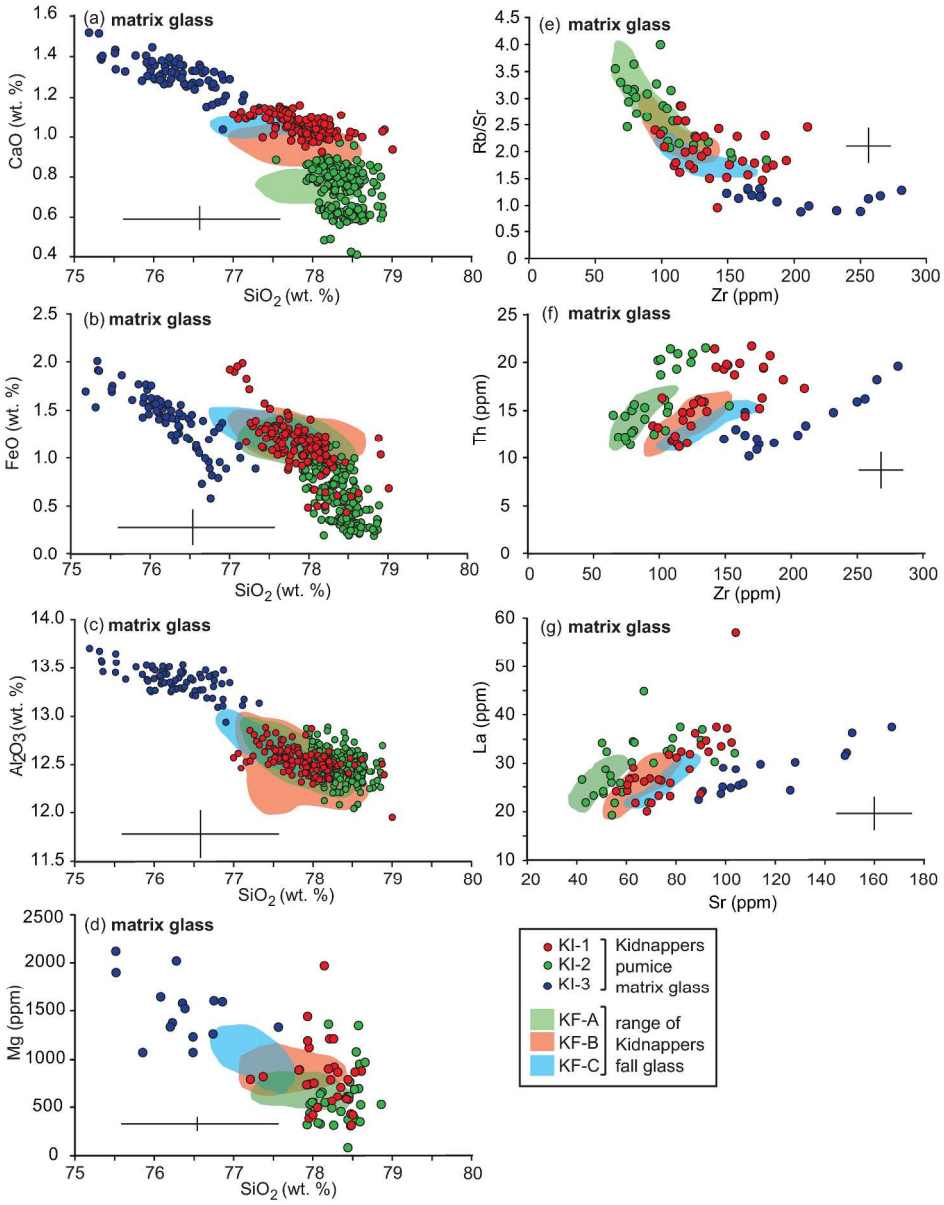


Fig. 6
239x307mm (300 x 300 DPI)

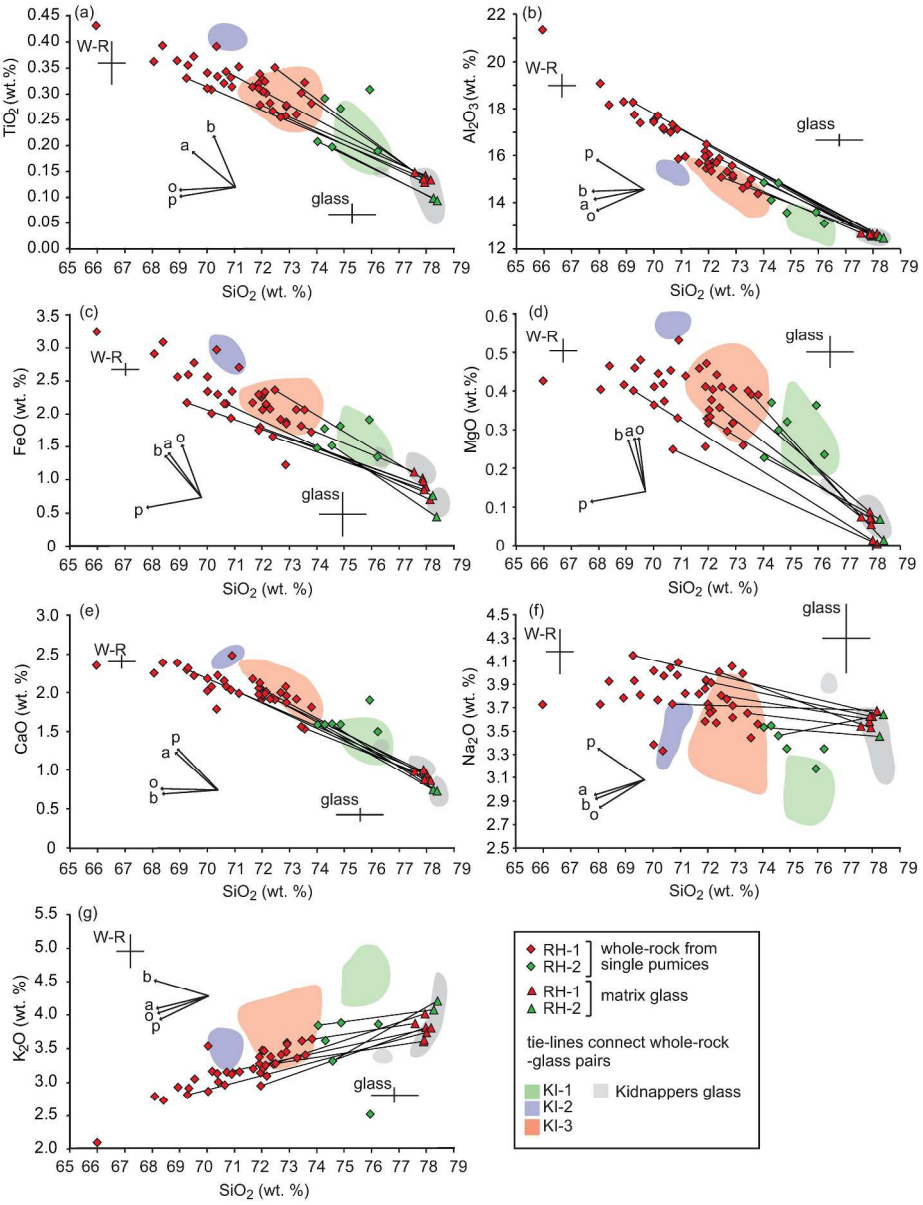


Fig. 7
258x338mm (300 x 300 DPI)

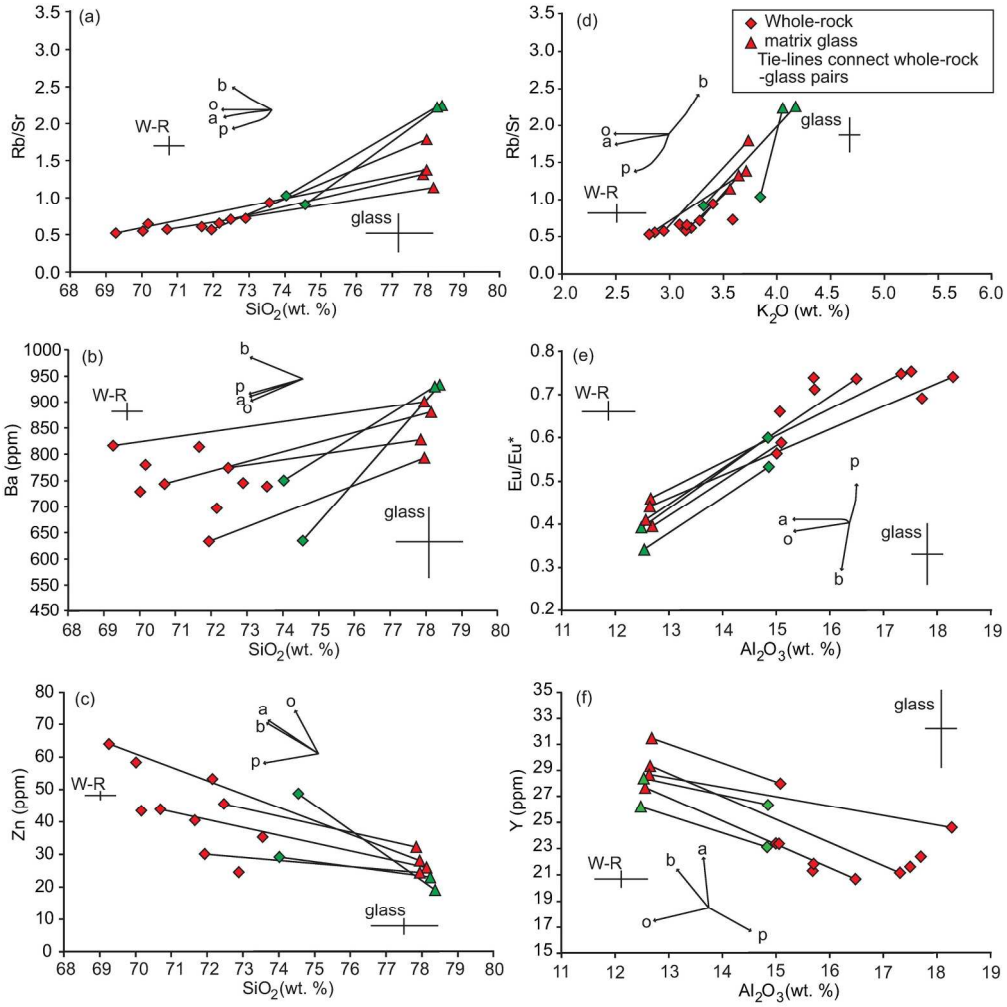


Fig. 8
202x202mm (300 x 300 DPI)

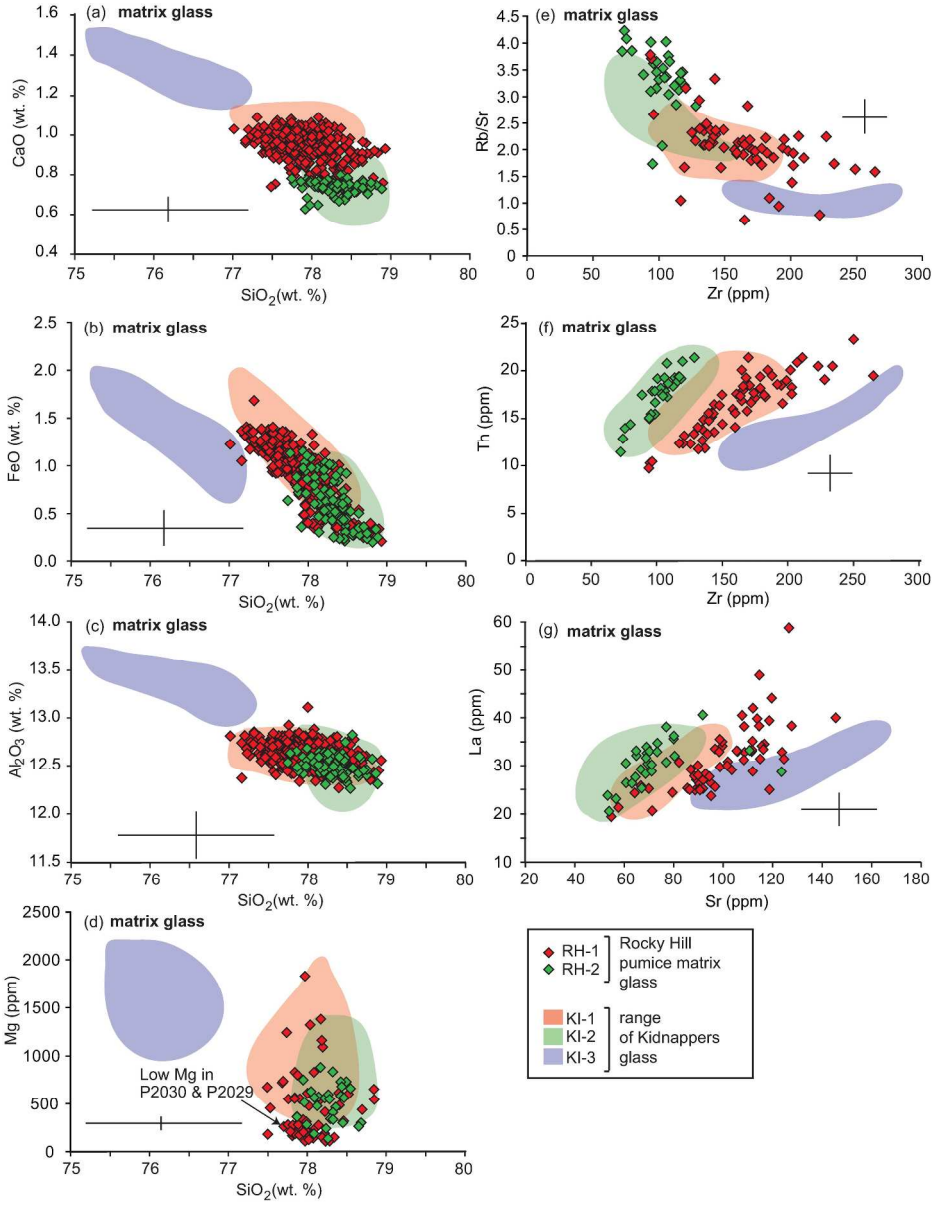


Fig. 9
260x336mm (300 x 300 DPI)

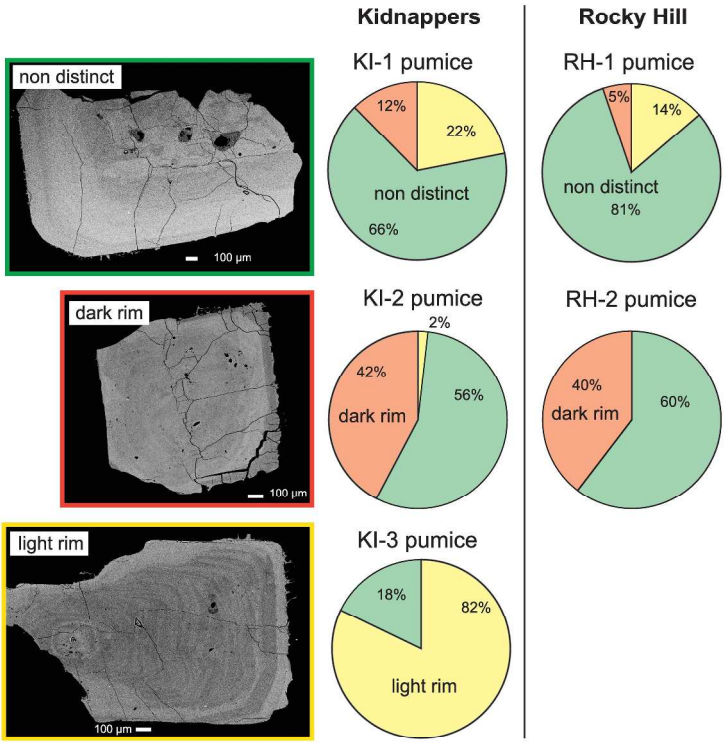


Fig. 10
297x420mm (300 x 300 DPI)

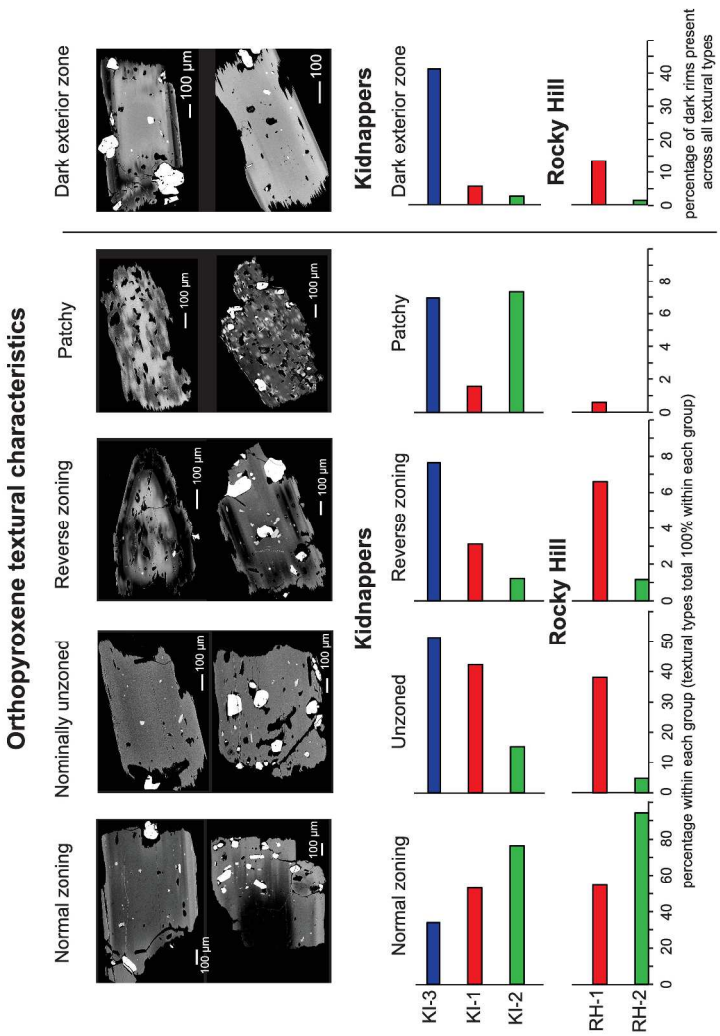


Fig. 11
297x420mm (300 x 300 DPI)

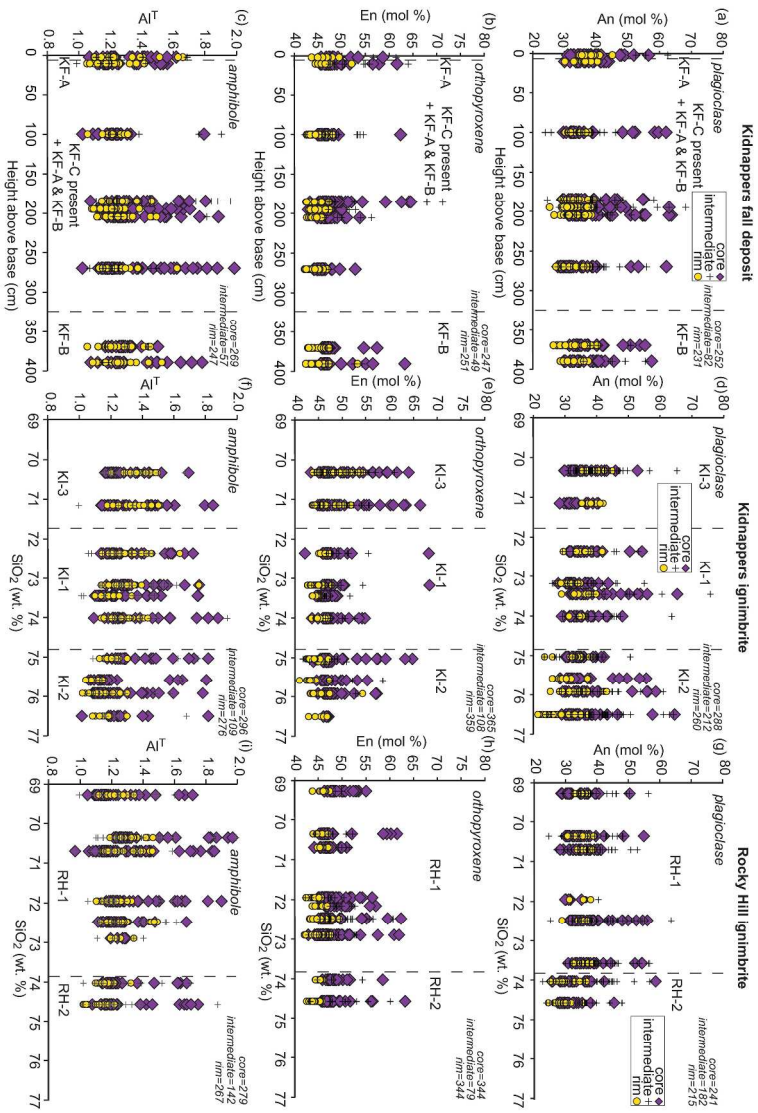


Fig. 12
297x420mm (300 x 300 DPI)

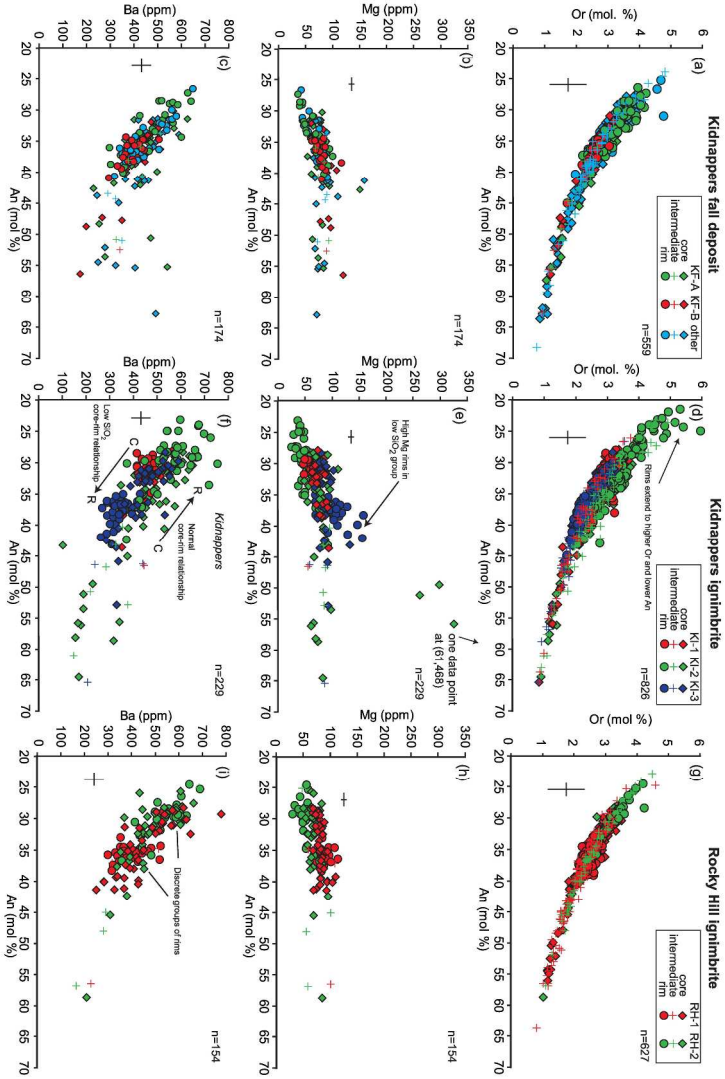


Fig. 13
297x420mm (300 x 300 DPI)

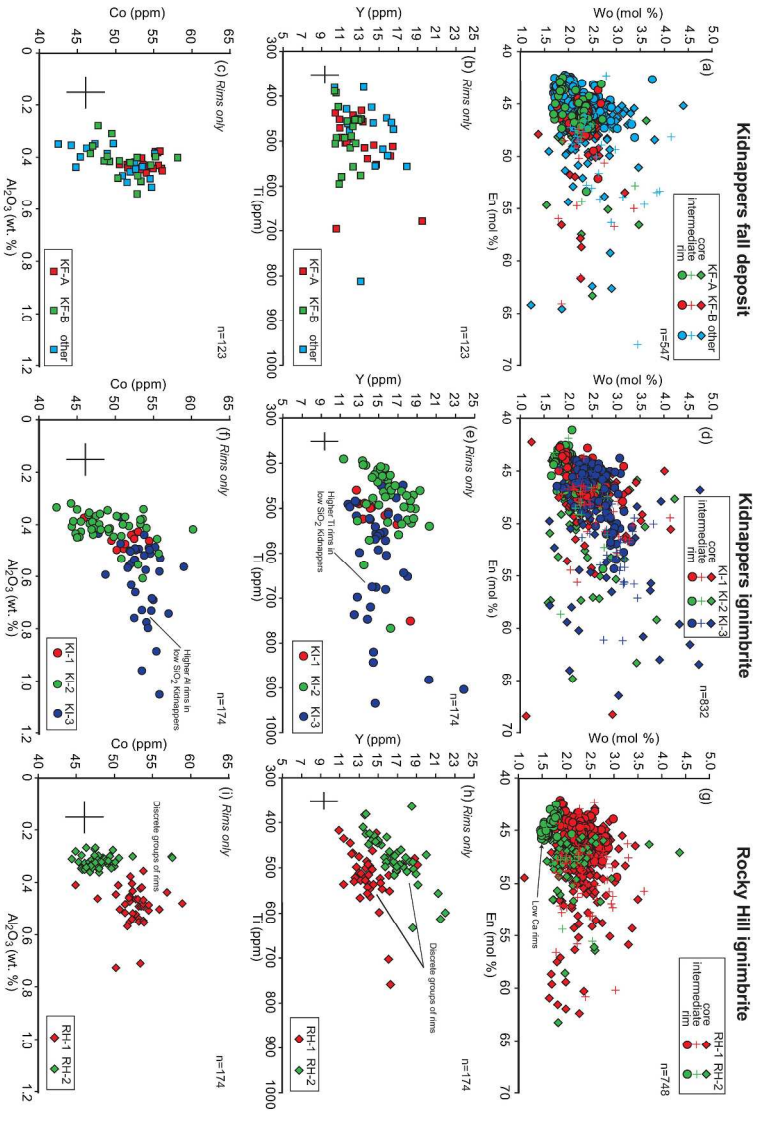


Fig. 14
297x420mm (300 x 300 DPI)

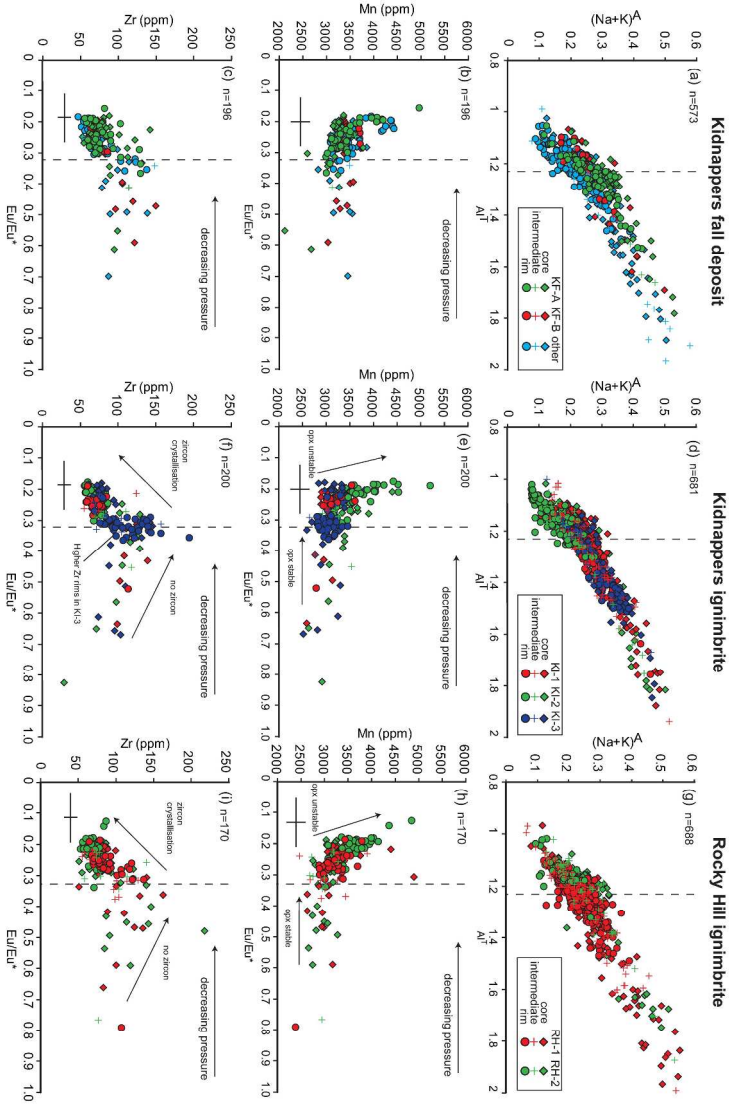


Fig. 15
297x420mm (300 x 300 DPI)

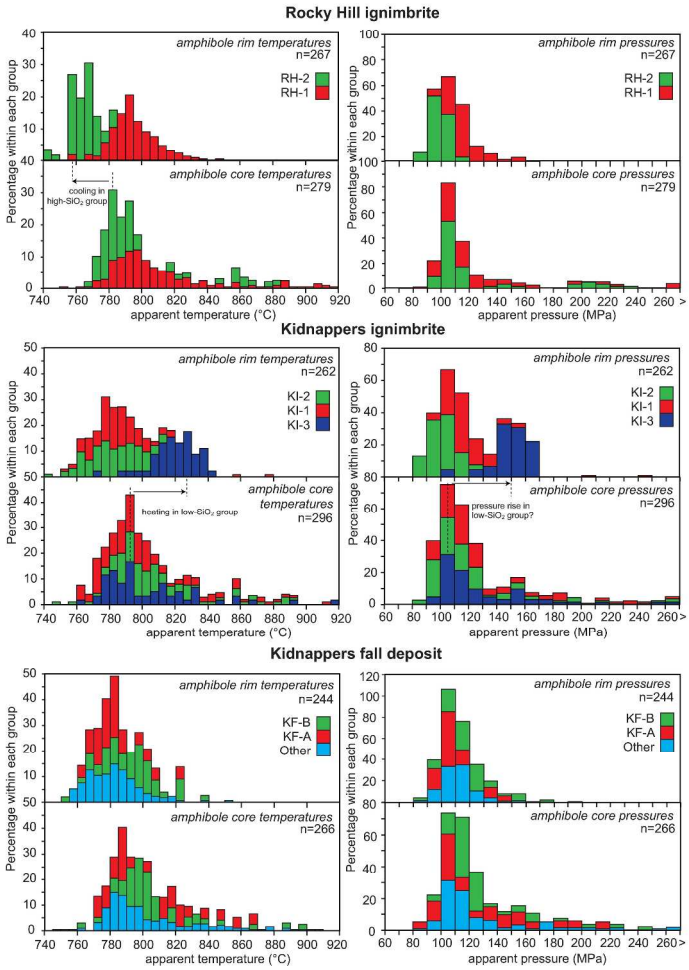


Fig. 16
297x420mm (300 x 300 DPI)

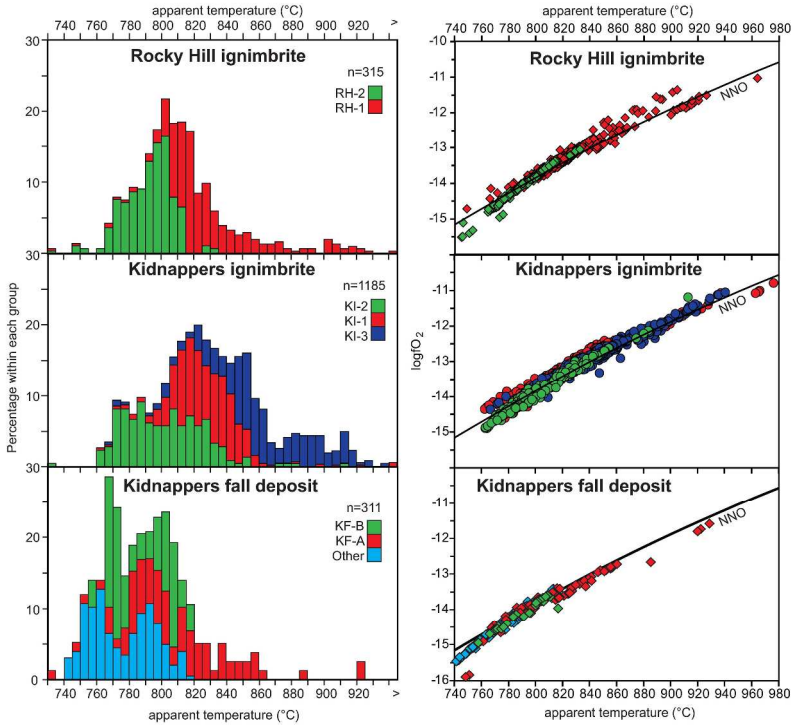


Fig. 17
297x420mm (300 x 300 DPI)

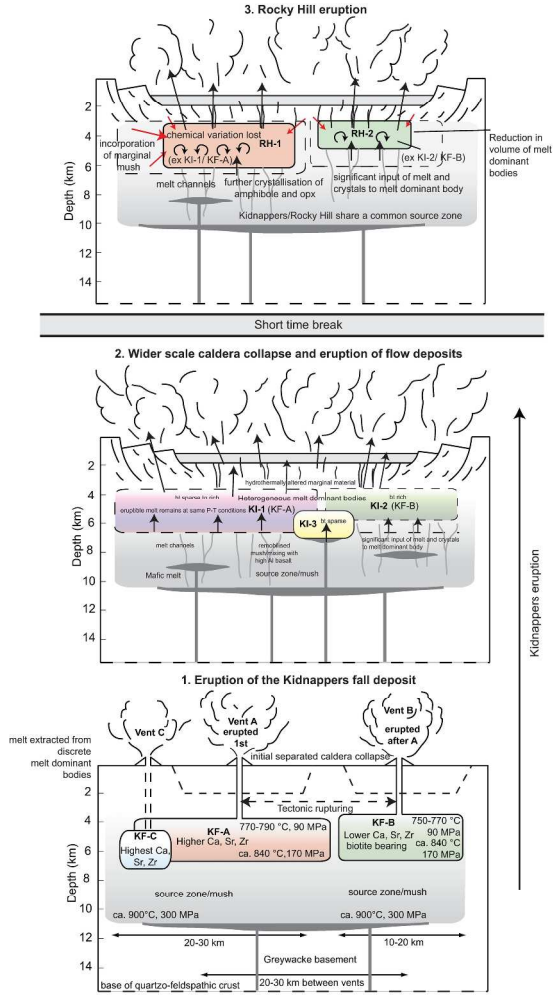


Fig. 18
290x287mm (300 x 300 DPI)

*Table 1: Mean whole-rock major and trace element concentrations for each compositional group within Kidnappers and Rocky Hill pumices*

| | Kidnappers pumice | | | | | | Rocky Hill pumice | | | |
|---|---|---|---|---|---|---|---|---|---|---|
| | KI-1 | | KI-2 | | KI-3 | | RH-1 | | RH-2 | |
| | 72-74 wt. % $SiO_2$ | | > 74.5 wt. % $SiO_2$ | | < 72 wt. % $SiO_2$ | | <74 wt. % $SiO_2$ | | > 74 wt. % $SiO_2$ | |
| | Mean | ± 2 sd | Mean | ± 2 sd | Mean | ± 2 sd | Mean | ± 2 sd | Mean | ± 2 sd |
| **Major elements** | | | | | | | | | | |
| **XRF** | *n=27* | | *n=12* | | *n=3* | | *n=37* | | *n=6* | |
| **$SiO_2$** | 73.0 | *1.30* | 75.6 | *1.07* | 70.8 | *0.63* | 71.4 | *2.99* | 75.0 | *1.79* |
| **$TiO_2$** | 0.30 | *0.05* | 0.21 | *0.09* | 0.41 | *0.03* | 0.32 | *0.07* | 0.24 | *0.11* |
| **$Al_2O_3$** | 14.4 | *1.06* | 13.1 | *0.77* | 15.3 | *0.69* | 16.3 | *2.39* | 14.0 | *1.45* |
| **$Fe_2O_3$ T** | 2.42 | *0.41* | 1.77 | *0.56* | 3.28 | *0.50* | 2.45 | *0.86* | 1.83 | *0.50* |
| **MnO** | 0.06 | *0.01* | 0.04 | *0.01* | 0.08 | *0.03* | 0.05 | *0.02* | 0.04 | *0.01* |
| **MgO** | 0.43 | *0.11* | 0.28 | *0.15* | 0.57 | *0.05* | 0.39 | *0.13* | 0.30 | *0.12* |
| **CaO** | 2.07 | *0.34* | 1.34 | *0.30* | 2.47 | *0.18* | 2.04 | *0.41* | 1.62 | *0.28* |
| **$Na_2O$** | 3.48 | *0.51* | 2.99 | *0.36* | 3.53 | *0.51* | 3.79 | *0.40* | 3.40 | *0.28* |
| **$K_2O$** | 3.85 | *0.61* | 4.58 | *0.48* | 3.54 | *0.51* | 3.21 | *0.50* | 3.50 | *1.06* |
| **$P_2O_5$** | 0.03 | *0.08* | 0.02 | *0.01* | 0.05 | *0.09* | 0.06 | *0.12* | 0.07 | *0.12* |
| **Totals normalised to 100%, volatile free** | | | | | | | | | | |
| **FeO T** | 2.17 | *0.37* | 1.59 | *0.51* | 2.95 | *0.45* | 2.21 | *0.78* | 1.64 | *0.45* |
| **LOI** | 1.96 | *1.74* | 2.57 | *0.87* | 2.76 | *0.97* | 3.55 | *1.50* | 3.22 | *0.94* |
| **Trace elements Solution ICP-MS** | *n=10* | | *n=7* | | *n=3* | | *n=10* | | *n=2* | |
| **Li** | 15.2 | *11.7* | 15.5 | *12.6* | 14.5 | *14.7* | 22.7 | *20.0* | 10.7 | *4.5* |
| **B** | 3.71 | *2.44* | 3.12 | *1.19* | 2.72 | *0.56* | 3.43 | *1.72* | 2.81 | *0.38* |
| **MgO wt. %** | 0.363 | *0.134* | 0.248 | *0.155* | 0.530 | *0.024* | 0.378 | *0.117* | 0.257 | *0.131* |
| **Sc** | 6.56 | *2.34* | 4.67 | *2.38* | 9.78 | *0.50* | 6.93 | *1.34* | 5.25 | *1.46* |
| **$TiO_2$ wt. %** | 0.256 | *0.055* | 0.188 | *0.106* | 0.371 | *0.028* | 0.313 | *0.068* | 0.215 | *0.036* |
| **V** | 17.6 | *6.7* | 10.7 | *8.9* | 25.2 | *2.1* | 20.0 | *3.9* | 15.1 | *2.8* |
| **Cr** | 2.15 | *1.78* | 1.16 | *0.80* | 2.39 | *1.59* | 1.96 | *0.64* | 2.27 | *2.37* |
| **Mn** | 392 | *36* | 301 | *97* | 722 | - | 361 | *173* | - | - |
| **Co** | 2.35 | *1.16* | 1.71 | *0.68* | 3.77 | *2.29* | 2.94 | *1.26* | 1.95 | *0.79* |
| **Ni** | 0.836 | *0.232* | 0.543 | *0.173* | 1.12 | *0.29* | 1.23 | *0.77* | 1.20 | *1.50* |
| **Cu** | 3.81 | *2.88* | 3.91 | *2.05* | 4.39 | *1.43* | 4.67 | *2.16* | 7.85 | *6.34* |
| **Zn** | 35.7 | *11.6* | 33.2 | *12.9* | 55.3 | *29.1* | 43.9 | *24.5* | 39.0 | *27.6* |
| **Ga** | 16.6 | *1.6* | 15.6 | *1.2* | 18.0 | *0.8* | 18.1 | *1.9* | 15.3 | *3.3* |
| **Rb** | 109 | *26* | 144 | *28* | 103 | *7* | 97.8 | *14* | 112 | *23* |
| **Sr** | 153 | *34* | 96 | *30* | 187 | *14* | 153 | *36* | 116 | *3* |
| **Y** | 23.9 | *4.5* | 25.1 | *3.8* | 27.9 | *2.2* | 22.8 | *4.4* | 24.7 | *4.5* |
| **Zr** | 104 | *28* | 85.0 | *33.9* | 172 | *42* | 116 | *17* | 89.7 | *19.0* |
| **Nb** | 8.22 | *0.74* | 8.31 | *1.57* | 9.64 | *0.36* | 9.79 | *1.05* | 7.82 | *2.05* |
| **Mo** | 1.43 | *0.66* | 1.60 | *0.57* | 1.46 | *0.45* | 1.35 | *0.49* | 1.76 | *0.23* |
| **Cs** | 6.37 | *2.11* | 8.95 | *2.23* | 5.09 | *1.29* | 5.94 | *1.04* | 6.55 | *1.31* |
| **Ba** | 729 | *79* | 791 | *116* | 718 | *132* | 747 | *109* | 692 | *163* |
| **La** | 23.3 | *5.3* | 26.5 | *2.5* | 24.6 | *3.9* | 22.9 | *4.5* | 24.5 | *8.8* |
| **Ce** | 47.0 | *7.2* | 52.3 | *5.3* | 52.5 | *9.6* | 48.4 | *10.9* | 47.1 | *12.0* |
| **Pr** | 5.51 | *1.54* | 6.07 | *0.69* | 5.93 | *0.85* | 5.19 | *0.99* | 5.72 | *1.42* |
| **Nd** | 20.6 | *5.8* | 22.0 | *3.0* | 22.7 | *2.9* | 19.0 | *3.7* | 20.8 | *4.9* |
| **Sm** | 4.22 | *1.19* | 4.38 | *0.74* | 4.79 | *0.48* | 3.82 | *0.72* | 4.22 | *0.92* |
| **Eu** | 0.93 | *0.23* | 0.71 | *0.16* | 1.14 | *0.12* | 0.86 | *0.15* | 0.78 | *0.00* |
| **Gd** | 4.13 | *1.04* | 4.21 | *0.62* | 4.81 | *0.45* | 3.81 | *0.68* | 4.24 | *0.53* |
| **Tb** | 0.631 | *0.161* | 0.634 | *0.113* | 0.739 | *0.099* | 0.596 | *0.114* | 0.628 | *0.08* |
| **Dy** | 3.96 | *0.88* | 4.03 | *0.68* | 4.69 | *0.42* | 3.77 | *0.68* | 4.02 | *0.55* |
| **Ho** | 0.826 | *0.165* | 0.842 | *0.142* | 0.971 | *0.089* | 0.783 | *0.145* | 0.827 | *0.137* |
| **Er** | 2.46 | *0.48* | 2.58 | *0.41* | 2.86 | *0.24* | 2.35 | *0.42* | 2.52 | *0.52* |
| **Tm** | 0.380 | *0.071* | 0.407 | *0.056* | 0.432 | *0.029* | 0.363 | *0.060* | 0.388 | *0.081* |
| **Yb** | 2.54 | *0.42* | 2.76 | *0.33* | 2.83 | *0.12* | 2.42 | *0.42* | 2.67 | *0.57* |

| | | | | | | | | | | |
|---|---|---|---|---|---|---|---|---|---|---|
| **Lu** | 0.384 | *0.062* | 0.424 | *0.058* | 0.428 | *0.010* | 0.367 | *0.055* | 0.394 | *0.080* |
| **Hf** | 3.14 | *0.62* | 2.89 | *0.90* | 4.68 | *0.84* | 3.62 | *0.62* | 2.74 | *0.05* |
| **Ta** | 0.677 | *0.205* | 0.751 | *0.142* | 0.715 | *0.182* | 0.788 | *0.117* | 0.777 | *0.322* |
| **W** | 1.17 | *0.58* | 1.42 | *0.68* | 1.20 | *0.76* | 1.24 | *0.61* | 1.55 | *0.56* |
| **Ti** | 1.28 | *0.65* | 1.48 | *0.48* | 1.42 | *0.80* | 1.36 | *0.62* | 1.96 | *1.27* |
| **Pb** | 12.7 | *2.4* | 13.5 | *2.7* | 18.6 | *6.9* | 15.9 | *4.3* | 14.3 | *7.0* |
| **Th** | 10.5 | *1.3* | 13.4 | *1.3* | 9.75 | *0.73* | 11.8 | *1.7* | 11.3 | *4.1* |
| **U** | 2.35 | *0.33* | 2.90 | *0.22* | 2.29 | *0.14* | 2.35 | *0.30* | 2.50 | *0.59* |
| **Eu/Eu*** | 0.67 | *0.10* | 0.50 | *0.09* | 0.73 | *0.03* | 0.67 | *0.15* | 0.57 | *0.10* |

*Table 2: Mean matrix glass major and trace element concentrations for each compositional group within Kidnappers and Rocky Hill pumices*

| | Kidnappers matrix glass | | | | | | Rocky Hill matrix glass | | | |
|---|---|---|---|---|---|---|---|---|---|---|
| | KI-1 | | KI-2 | | KI-3 | | RH-1 | | RH-2 | |
| | Mean | ± 2 sd | Mean | ± 2 sd | Mean | ± 2 sd | Mean | ± 2 sd | Mean | ± 2 sd |
| **Major elements** | | | | | | | | | | |
| **EPMA** | *n=125* | | *n=193* | | *n=76* | | *n=412* | | *n=95* | |
| **$SiO_2$** | 77.9 | *0.7* | 78.4 | *0.5* | 76.3 | *1.0* | 77.9 | *0.6* | 78.3 | *0.5* |
| **$TiO_2$** | 0.136 | *0.042* | 0.081 | *0.047* | 0.153 | *0.039* | 0.137 | *0.036* | 0.096 | *0.024* |
| **$Al_2O_3$** | 12.5 | *0.3* | 12.5 | *0.3* | 13.4 | *0.3* | 12.6 | *0.2* | 12.5 | *0.2* |
| **$Fe_2O_3$ T** | 1.15 | *0.54* | 0.62 | *0.51* | 1.38 | *0.59* | 0.94 | *0.56* | 0.63 | *0.52* |
| **MnO** | 0.031 | *0.039* | 0.025 | *0.036* | 0.047 | *0.044* | 0.017 | *0.032* | 0.017 | *0.028* |
| **MgO** | 0.104 | *0.043* | 0.046 | *0.057* | 0.153 | *0.063* | 0.057 | *0.082* | 0.045 | *0.069* |
| **CaO** | 1.06 | *0.11* | 0.73 | *0.22* | 1.31 | *0.17* | 0.95 | *0.13* | 0.74 | *0.06* |
| **$Na_2O$** | 3.48 | *0.50* | 3.39 | *0.50* | 3.91 | *0.40* | 3.61 | *0.26* | 3.53 | *0.37* |
| **$K_2O$** | 3.64 | *0.37* | 4.25 | *0.73* | 3.40 | *0.38* | 3.77 | *0.35* | 4.13 | *0.23* |
| **Raw uncorrected total** | 95.0 | | 95.7 | | 96.4 | | 95.8 | | 95.9 | |
| **Trace elements** | | | | | | | | | | |
| **LA-ICP-MS** | *n=32* | | *n=29* | | *n=16* | | *n=61* | | *n=29* | |
| **Li** | 42.1 | *20.5* | 36.7 | *16.9* | 34.8 | *17.0* | 47.2 | *20.5* | 52.3 | *13.7* |
| **$Na_2O$ wt. %** | 3.65 | *0.56* | 3.36 | *0.66* | 3.72 | *1.67* | 4.01 | *1.08* | 3.88 | *0.75* |
| **MgO wt. %** | 0.145 | *0.168* | 0.102 | *0.095* | 0.268 | *0.178* | 0.076 | *0.120* | 0.083 | *0.066* |
| **CaO wt. %** | 1.01 | *0.51* | 0.88 | *0.41* | 1.38 | *0.61* | 1.06 | *0.30* | 0.87 | *0.41* |
| **Sc** | 9.64 | *7.35* | 6.10 | *11.53* | 10.5 | *6.5* | 9.69 | *4.03* | 7.02 | *1.75* |
| **$TiO_2$ wt. %** | 0.17 | *0.05* | 0.12 | *0.04* | 0.23 | *0.09* | 0.18 | *0.13* | 0.12 | *0.01* |
| **V** | 2.08 | *2.36* | 1.35 | *2.12* | 2.76 | *2.77* | 3.06 | *3.41* | 1.34 | *0.50* |
| **Mn** | 204 | *116* | 242 | *122* | 356 | *134* | 146 | *57* | 154 | *64* |
| **Co** | 1.04 | *1.89* | 0.540 | *2.044* | 1.21 | *2.66* | 1.07 | *1.82* | 0.28 | *1.17* |
| **Ni** | 1.47 | *6.13* | 1.30 | *6.65* | 1.75 | *5.78* | 0.75 | *4.04* | 0.84 | *5.14* |
| **Cu** | 5.66 | *24.84* | 4.66 | *35.89* | 6.26 | *42.51* | 9.15 | *28.06* | - | - |
| **Zn** | 28.4 | *21.2* | 25.7 | *18.4* | 36.2 | *22.8* | 27.3 | *34.0* | 21.5 | *21.5* |
| **Ga** | 16.4 | *5.8* | 15.8 | *4.5* | 15.6 | *5.3* | 17.0 | *5.6* | 15.6 | *3.0* |
| **Rb** | 153 | *58* | 169 | *35* | 131 | *56* | 133 | *45* | 158 | *18* |
| **Sr** | 79.1 | *28.1* | 64.4 | *32.60* | 117 | *49* | 100 | *36* | 72.64 | *30.12* |
| **Y** | 32.5 | *42.1* | 27.1 | *14.0* | 28.1 | *15.6* | 29.8 | *13.4* | 27.5 | *8.9* |
| **Zr** | 140 | *60* | 102 | *55* | 201 | *86* | 164 | *72* | 101 | *28* |
| **Nb** | 9.98 | *2.89* | 9.49 | *2.71* | 10.5 | *2.4* | 10.8 | *4.6* | 8.92 | *1.39* |
| **Mo** | 2.16 | *3.91* | 1.84 | *2.36* | 1.68 | *1.99* | 1.72 | *0.86* | 1.87 | *1.19* |
| **Cs** | 8.16 | *3.58* | 8.51 | *2.78* | 6.41 | *2.24* | 7.42 | *1.82* | 8.51 | *3.08* |
| **Ba** | 856 | *204* | 868 | *184* | 827 | *164* | 860 | *215* | 930 | *159* |
| **La** | 30.7 | *20.6* | 29.3 | *11.9* | 28.1 | *9.1* | 31.2 | *14.0* | 30.6 | *9.0* |
| **Ce** | 57.0 | *14.9* | 54.9 | *10.0* | 54.4 | *11.4* | 56.2 | *14.3* | 57.5 | *10.2* |
| **Pr** | 6.71 | *6.03* | 6.09 | *1.92* | 5.92 | *2.11* | 6.15 | *2.12* | 6.24 | *1.49* |
| **Nd** | 27.4 | *36.3* | 23.4 | *14.2* | 25.6 | *9.4* | 24.5 | *9.2* | 23.9 | *7.2* |
| **Sm** | 5.81 | *11.08* | 4.51 | *3.42* | 4.93 | *3.31* | 4.93 | *2.02* | 4.77 | *2.02* |
| **Eu** | 0.694 | *1.095* | 0.631 | *0.710* | 0.818 | *0.496* | 0.662 | *0.291* | 0.507 | *0.235* |
| **Gd** | 5.17 | *8.47* | 3.83 | *3.93* | 4.63 | *4.04* | 4.69 | *2.40* | 4.16 | *1.72* |
| **Tb** | 0.804 | *1.392* | 0.613 | *0.518* | 0.772 | *0.436* | 0.731 | *0.369* | 0.681 | *0.253* |
| **Dy** | 5.85 | *8.02* | 4.28 | *3.03* | 5.35 | *3.35* | 4.91 | *2.30* | 4.48 | *1.60* |
| **Ho** | 1.21 | *1.63* | 1.01 | *0.66* | 1.15 | *0.91* | 1.06 | *0.57* | 0.93 | *0.38* |
| **Er** | 3.45 | *4.04* | 2.93 | *2.07* | 2.85 | *2.38* | 3.18 | *1.53* | 2.95 | *1.14* |
| **Tm** | 0.518 | *0.706* | 0.427 | *0.448* | 0.540 | *0.385* | 0.495 | *0.246* | 0.501 | *0.208* |
| **Yb** | 3.74 | *4.10* | 2.96 | *2.23* | 2.70 | *2.85* | 3.48 | *1.82* | 3.35 | *1.27* |
| **Lu** | 0.573 | *0.688* | 0.513 | *0.385* | 0.537 | *0.418* | 0.550 | *0.254* | 0.571 | *0.299* |
| **Hf** | 4.11 | *2.47* | 3.38 | *2.11* | 5.47 | *3.45* | 5.02 | *2.48* | 3.68 | *1.37* |
| **Ta** | 0.903 | *0.565* | 0.941 | *0.602* | 0.859 | *0.495* | 0.993 | *0.422* | 0.979 | *0.304* |
| **W** | 2.10 | *1.52* | 2.25 | *1.76* | 1.74 | *1.52* | 2.23 | *1.87* | 2.21 | *0.88* |
| **Pb** | 17.5 | *3.2* | 17.1 | *6.1* | 20.3 | *6.2* | 21.5 | *7.0* | 19.1 | *4.3* |
| **Th** | 16.0 | *6.3* | 16.3 | *6.8* | 13.7 | *5.4* | 16.4 | *6.1* | 17.4 | *4.8* |
| **U** | 3.55 | *1.49* | 3.73 | *1.31* | 3.08 | *0.75* | 3.36 | *0.67* | 3.71 | *0.79* |

| | | | | | | | | | | |
|---|---|---|---|---|---|---|---|---|---|---|
| **Rb/Sr** | 2.81 | *4.95* | 1.00 | *14.73* | 2.73 | *10.40* | 1.82 | *1.18* | 2.79 | *1.83* |
| **Eu/Eu*** | 0.45 | *0.47* | 0.45 | *0.56* | 0.53 | *0.27* | 0.43 | *0.19* | 0.36 | *0.23* |

*Table 3: Summary of mineral characteristics and features from all deposits*

| | Phenocryst size | Characteristics | Notable features |
|---|---|---|---|
| **Plagioclase** | ≤ 2mm | Euhedral to subhedral | Variable and complex zoning |
| **Orthopyroxene** | ≤ 1mm | Subhedral, fractured with ragged terminations | Near ubiquitous Fe-Ti oxide inclusions ± zircon & apatite |
| **Quartz** | ≤ 2mm | Euhedral, bipyramidal, often broken | Variable and complex zoning in CL |
| **Amphibole** | ≤ 3mm (Kid)<br>≤ 5mm (RH) | Euhedral, prismatic | Fe-Ti oxide inclusions common ± apatite |
| **Biotite** | ≤ 1mm | Euhedral to subhedral books and flakes | Golden coloured and weathered,<br>'fresher' in RH<br>No clear zoning |
| **Fe-Ti oxides** | ≤ 200μm | Discrete oxides altered and oxidized | |

*Table 4: Range and average mineral compositions from each compositional group*

| Deposit | Kidnappers fall deposit | | Kidnappers ignimbrite | | | Rocky Hill ignimbrite | |
|---|---|---|---|---|---|---|---|
| Group | KF-A | KF-B | KI-1 | KI-2 | KI-3 | RH-1 | RH-2 |
| **Plagioclase** | | | | | | | |
| Total range | $An_{31}$ $Or_{0.9}$-$An_{63}$ $Or_{3.2}$ | $An_{26}$ $Or_{1.1}$-$An_{57}$ $Or_{4.2}$ | $An_{26}$ $Or_{0.8}$-$An_{65}$ $Or_{3.8}$ | $An_{21}$ $Or_{0.9}$-$An_{65}$ $Or_{6.0}$ | $An_{27}$ $Or_{0.8}$-$An_{65}$ $Or_{3.6}$ | $An_{25}$ $Or_{0.8}$-$An_{64}$ $Or_{4.6}$ | $An_{23}$ $Or_{1.0}$-$An_{59}$ $Or_{4.5}$ |
| Core average | $An_{39}$ $Or_{2.4}$ | $An_{37}$ $Or_{2.7}$ | $An_{37}$ $Or_{2.6}$ | $An_{36}$ $Or_{2.8}$ | $An_{35}$ $Or_{2.7}$ | $An_{36}$ $Or_{2.5}$ | $An_{33}$ $Or_{2.9}$ |
| Rim average | $An_{37}$ $Or_{2.5}$ | $An_{33}$ $Or_{3.1}$ | $An_{35}$ $Or_{2.7}$ | $An_{30}$ $Or_{3.7}$ | $An_{38}$ $Or_{2.2}$ | $An_{36}$ $Or_{2.4}$ | $An_{30}$ $Or_{3.3}$ |
| **Orthopyroxene** | | | | | | | |
| Total range | $En_{44}Wo_{2.0}$-$En_{61}Wo_{2.2}$ | $En_{42}Wo_{1.5}$-$En_{63}Wo_{3.6}$ | $En_{42}Wo_{1.1}$-$En_{68}Wo_{4.1}$ | $En_{41}Wo_{1.6}$-$En_{65}Wo_{5.2}$ | $En_{43}Wo_{1.6}$-$En_{66}Wo_{4.8}$ | $En_{42}Wo_{0.8}$-$En_{62}Wo_{3.6}$ | $En_{43}Wo_{1.5}$-$En_{63}Wo_{4.4}$ |
| Core average | $En_{49}Wo_{2.5}$ | $En_{48}Wo_{2.5}$ | $En_{48}Wo_{2.5}$ | $En_{48}Wo_{2.5}$ | $En_{49}Wo_{2.6}$ | $En_{48}Wo_{2.4}$ | $En_{48}Wo_{2.2}$ |
| Rim average | $En_{47}Wo_{2.4}$ | $En_{46}Wo_{2.2}$ | $En_{45}$ $Wo_{2.3}$ | $En_{44}$ $Wo_{2.1}$ | $En_{47}Wo_{2.5}$ | $En_{45}$ $Wo_{3.4}$ | $En_{45}$ $Wo_{1.6}$ |
| **Amphibole** | | | | | | | |
| Total range | 1.07-1.7 $Al^T$ | 1.05-1.78 $Al^T$ | 1.01-1.94 $Al^T$ | 1.02-1.82 $Al^T$ | 0.99-1.85 $Al^T$ | 0.97-1.99 $Al^T$ | 1.02-1.87 $Al^T$ |
| Core average | 1.31 $Al^T$ | 1.31 $Al^T$ | 1.30 $Al^T$ | 1.28 $Al^T$ | 1.31 $Al^T$ | 1.29 $Al^T$ | 1.27 $Al^T$ |
| Rim average | 1.20 $Al^T$ | 1.26 $Al^T$ | 1.26 $Al^T$ | 1.15 $Al^T$ | 1.42 $Al^T$ | 1.24 $Al^T$ | 1.13 $Al^T$ |
| **Magnetite** | | | | | | | |
| Total range | $Usp_{0.27-0.46}$ | $Usp_{0.29-0.38}$ | $Usp_{0.23-0.49}$ | $Usp_{0.27-0.36}$ | $Usp_{0.24-0.42}$ | $Usp_{0.23-0.48}$ | $Usp_{0.16-0.32}$ |
| Average | $Usp_{0.33}$ | $Usp_{0.30}$ | $Usp_{31}$ | $Usp_{31}$ | $Usp_{35}$ | $Usp_{31}$ | $Usp_{28}$ |
| **Ilmenite** | | | | | | | |
| Total range | $Ilm_{0.88-0.93}$ | $Ilm_{0.88-0.91}$ | $Ilm_{0.85-0.90}$ | $Ilm_{0.80-0.90}$ | $Ilm_{0.86-0.91}$ | $Ilm_{0.80-0.90}$ | $Ilm_{0.84-0.91}$ |
| Average | $Ilm_{0.89}$ | $Ilm_{0.89}$ | $Ilm_{0.88}$ | $Ilm_{0.89}$ | $Ilm_{0.88}$ | $Ilm_{0.88}$ | $Ilm_{0.89}$ |

*Table 5: Summary of model temperature, pressure and oxygen fugacity estimates*

| | Kidnappers fall deposit | | Kidnappers ig. | | | Rocky Hill ig. | |
|---|---|---|---|---|---|---|---|
| | **KF-A** | **KF-B** | **KI-1** | **KI-2** | **KI-3** | **RH-1** | **RH-2** |
| **Amphibole** | | | | | | | |
| **Ridolfi et al., 2010** | Uncertainty: temp: ±22 °C (σest), pressure: 11-24 % | | | | | | |
| Core average T (°C) | 805 | 810 | 800 | 805 | 805 | 810 | 800 |
| Rim average T (°C) | 780 | 795 | 785 | 780 | 820 | 795 | 765 |
| Core average P (MPa) | 130 | 135 | 130 | 125 | 130 | 130 | 125 |
| Rim average P (MPa) | 110 | 120 | 120 | 100 | 150 | 115 | 100 |
| **Putirka, 2016** | Uncertainty: eqn. 5: ±30 °C (SEE), eqn. 9: ±39 °C (SEE), eqn. 7a: 1.0 kbar | | | | | | |
| Core average T (°C) eqn. 5 | 790 | 795 | 785 | 785 | 790 | 790 | 782 |
| Rim average T (°C) eqn. 5 | 770 | 785 | 770 | 750 | 800 | 775 | 745 |
| Core average T (°C) eqn. 9 | 805 | 805 | 800 | 790 | 805 | 800 | 785 |
| Rim average T (°C) eqn. 9 | 790 | 790 | 790 | 770 | 815 | 790 | 765 |
| Core average P (MPa) eqn. 7a | 290 | 340 | 320 | 360 | 280 | 310 | 330 |
| Rim average P (MPa) eqn. 7a | 330 | 340 | 320 | 400 | 220 | 300 | 380 |
| **Fe-Ti oxides** | | | | | | | |
| **Ghiorso & Evans, 2008** | Uncertainty: ±50 °C (2σ; Hora et al., 2013) | | | | | | |
| Average T (°C) | 810 | 785 | 830 | 800 | 860 | 830 | 790 |
| Average Log $fO_2$ | -13.7 | -14.2 | -13.1 | -13.9 | -12.5 | -13.2 | -14.0 |
| **Plagioclase-melt** | | | | | | | |
| **Putirka, 2008** | Uncertainty: ±36 °C (SEE) | | | | | | |
| Rim average T (°C) | - | - | 780 | 750 | 820 | 785 | 760 |
| **Orthopyroxene-melt** | | | | | | | |
| **Putirka, 2008** | Uncertainty: ±41 °C (SEE) | | | | | | |
| Rim average T (°C) | - | - | 775 | 750 | 795 | 770 | 760 |

Uncertainties are those reported in the original studies unless otherwise stated. SEE = standard error of estimate, aad = average absolute deviation.